SANDIA REPORT

SAND2016-7260 Unlimited Release Printed July 26, 2016

Lagrangian Material Tracers (LMT) for Simulating Material Damage in ALEGRA

J.J. Sanchez, C.B. Luchini, O.E. Strack

Prepared by Sandia National Laboratories Albuquerque, New Mexico 87185 and Livermore, California 94550

Sandia National Laboratories is a multi-program laboratory managed and operated by Sandia Corporation, a wholly owned subsidiary of Lockheed Martin Corporation, for the U.S. Department of Energy's National Nuclear Security Administration under contract DE-AC04-94AL85000.

Approved for public release; further dissemination unlimited.



A CONTRACTOR

Issued by Sandia National Laboratories, operated for the United States Department of Energy by Sandia Corporation.

NOTICE: This report was prepared as an account of work sponsored by an agency of the United States Government. Neither the United States Government, nor any agency thereof, nor any of their employees, nor any of their contractors, subcontractors, or their employees, make any warranty, express or implied, or assume any legal liability or responsibility for the accuracy, completeness, or usefulness of any information, apparatus, product, or process disclosed, or represent that its use would not infringe privately owned rights. Reference herein to any specific commercial product, process, or service by trade name, trademark, manufacturer, or otherwise, does not necessarily constitute or imply its endorsement, recommendation, or favoring by the United States Government, any agency thereof, or any of their contractors or subcontractors. The views and opinions expressed herein do not necessarily state or reflect those of the United States Government, any agency thereof, or any of their contractors.

Printed in the United States of America. This report has been reproduced directly from the best available copy.

Available to DOE and DOE contractors from U.S. Department of Energy Office of Scientific and Technical Information P.O. Box 62

Oak Ridge, TN 37831

Telephone: (865) 576-8401 Facsimile: (865) 576-5728

E-Mail: reports@adonis.osti.gov
Online ordering: http://www.osti.gov/bridge

Available to the public from

U.S. Department of Commerce National Technical Information Service 5285 Port Royal Rd Springfield, VA 22161

Telephone: (800) 553-6847 Facsimile: (703) 605-6900

E-Mail: orders@ntis.fedworld.gov

Online ordering: http://www.ntis.gov/help/ordermethods.asp?loc=7-4-0#online



SAND2016-7260 Unlimited Release Printed July 26, 2016

Lagrangian Material Tracers (LMT) for Simulating Material Damage in ALEGRA

Jason J. Sanchez
Computational Shock and Multiphysics
Sandia National Laboratories
Albuquerque, NM 87185-1323
jassanc@sandia.gov

Chris B. Luchini
Computational Shock and Multiphysics
Sandia National Laboratories
Albuquerque, NM 87185-1323
cbluchi@sandia.gov

O. Erik Strack
Scaleable Algorithms
Sandia National Laboratories
Albuquerque, NM 87185-1318
oestrac@sandia.gov

Abstract

A method for providing non-diffuse transport of material quantities in arbitrary Lagrangian-Eulerian (ALE) dynamic solid mechanics computations is presented. ALE computations are highly desirable for simulating dynamic problems that incorporate multiple materials and large deformations. Despite the advantages of using ALE for such problems, the method is associated with diffusion of material quantities due to the advection transport step of the computational cycle. This drawback poses great difficulty for applications of material failure for which discrete features are important, but are smeared out as a result of the diffusive advection operation. The focus of this work is an ALE method that incorporates transport of variables on discrete, massless points that move with the velocity field, referred to as Lagrangian material tracers (LMT), and consequently prevents diffusion of certain material quantities of interest. A detailed description of the algorithm is provided along with discussion of its computational aspects. Simulation results include a simple proof of concept, verification using a manufactured solution, and fragmentation of a uniformly loaded thin ring that clearly demonstrates the improvement offered by the ALE LMT method.

Acknowledgment

This work was supported by the U.S. Army Research Laboratory and DOE's National Nuclear Security Administration.

The authors gratefully acknowledge Professor Rebecca Brannon of the University of Utah for establishing the project that supported this work. Her insistence in 2006 that corruption of material model state variables by ALE codes was a major cause of their lack of predictive capability and her belief that any improvement to the ALE approach that could preserve those properties would have an improved chance of success inspired this work.

Contents

1	Intr	roduction	7
2	Gov	verning Continuum Equations of a Deformable Solid	9
3	The	e ALE LMT Method	10
	3.1	Spatial Discretization for ALE LMT	10
	3.2	The Lagrangian Step	12
	3.3	The Remap Step	14
4	AL	E LMT Simulations	17
	4.1	Proof of Concept: Rigid Body Motion With Initial Damage	18
	4.2	Code Verification: Generalized Vortex Manufactured Solution	19
	4.3	Application: Simulation of a Rotating and Expanding Ring	26
5	Cor	nclusions	32
Aı	ppen	dix	
A	Ger	neralized Vortex Manufactured Solution	33
R	eferer	nces	40
T7.			
F)	igur	ees	
	1	Spatial discretization of ALE LMT	10
	2	Local arrangement of 2D quadrilateral elements considered for remapping of ele-	1.5
	2	ment centered variables in Ω_e	15
	3	Discretization of a single remap sweep direction, $\alpha = 1,, nd$, for 2D element Ω_e	15
	4	Illustration of swept material volumes across the faces (shaded areas) of a 2D quadrilateral element Ω_e	17
	5	Bar rotation problem with prescribed initial damage: Comparison of ALE & ALE	1 /
	5	LMT damage results (blue correspond to $D = 0$ and red corresponds to $D = 1$)	18
	6	Bar rotation problem with prescribed initial damage at $t = 10t_p$ with Lagrangian	10
	U	material tracers displayed	20
	7	Initial configuration of generalized vortex problem	21
	8	ALE LMT discretization of the generalized vortex problem $(n = 1, p = 3)$	22
	9	Comparison between the exact (left) and ALE LMT (right) velocity magnitude	22
		solutions for the generalized vortex problem with a radial mesh $(n = 1, p = 3)$	23
	10	Comparison between the exact (left) and ALE LMT (right) velocity magnitude	23
	10	solutions for the generalized vortex problem with a rectangular mesh $(n = 1, p = 3)$.	24
	11	ALE LMT velocity solution error at $t = 0.25 s$ for radial mesh	25
	12	ALE LMT velocity solution error at $t = 0.25 s$ for rectangular mesh	2525
	13	Eulerian mesh of cells for expanding ring problems: $16,920$ cells	26
	14	Comparison of spatial variation of σ_{v} for ALE (left) and ALE LMT (right); 63.2 MPa \leq	
	14	Comparison of spatial variation of o_y for ALE (left) and ALE Livit (right), 03.2 MT $a \le \sigma_y \le 88.2 MPa$	29

15	Close up view of a ring sector comparing spatial variation of σ_y between ALE	
	(left) and ALE LMT (right) $63.2MPa \le \sigma_y \le 88.2MPa$	30
16	Comparison of equivalent plastic strain (red corresponds to $\bar{\epsilon}_p \ge 0.5$) for ALE (left)	
	and ALE LMT (right)	31

Tables

1 Introduction

The ability to predict material failure is important for many solid mechanics applications. The computational means employed for this purpose incorporate one or more of the numerous inelastic material models available to predict the evolution of plastic strain or damage that precede material failure. Generally speaking, failure of a real material subject to a uniform load is initiated at points of weakness introduced by inhomogeneities in the material that exist at the micro scale. That is, a geometrically uniform structure subjected to uniform loading will experience local deformation and failure. This feature of real material failure is not captured in a simulation by simply applying a continuum plasticity or damage model to a uniformly loaded structure. Such a simulation would predict simultaneous uniform failure of the entire structure (provided the numerical implementation is not sensitive to numerical roundoff, which can lead to localization). One method used to appropriately simulate material failure initiation is to introduce a statistical spatial variation of material properties, such as the yield or ultimate tensile strength, into the computational domain to capture the effect of local weakness attributed to micro structural material inhomogeneity. This approach has proven successful for predicting the initiation of failure of geometrically uniform structures subjected to uniform loading that compare favorably to experimental observations [1, 2].

ALE computational methods [3, 4, 5] are ideal for dynamic solid mechanics problems that include large deformations, multiple materials and complex geometries. Material is able to move through an arbitrary spatial mesh of elements without the problems that accompany high mesh distortion and tangling associated with pure Lagrangian Finite Element Methods (FEM). In general the ALE computational cycle consists of three steps; the FEM Lagrangian step, the re-meshing step and the advection (or remap) step. If a single mesh is used the re-meshing step is not performed, and the computation is considered to be (effectively) Eulerian. The solution obtained from the Lagrangian step is then remapped from the deformed mesh to the original mesh. Remapping algorithms [5] provide the transport of node and element quantities that make ALE calculations possible, however the remapping operation is diffusive, which causes smearing of the data being transported. The diffusive nature of advection transport drastically reduces the effectiveness of modeling real material failure using the aforementioned approach because the initial spatial variation of material properties is immediately washed out. The resolution of this issue is the focus of the research presented in this paper.

Particle-in-cell computational methods in solid mechanics, such as the material point method (MPM) [6], operate on the same principle of material transport as ALE methods; material is transported through an arbitrary spatial mesh of elements. The difference is the transport mechanism. ALE utilizes remapping algorithms and MPM relies on the motion of discrete particles for the transport of mass, the deformation gradient, and the material data. The concept of particle transport offers a non-diffusive method of moving data through the mesh. This work applies this transport method to ALE computations through the introduction of discrete, massless points referred to as Lagrangian material tracers (LMT). These tracers are associated with the material inserted into the mesh and are used to transport quantities associated with the constitutive behavior of the material and include the deformation gradient, stress tensor, and history variables. These variables

are not only carried and updated on the tracers, but their values are aggregated to the elements in the mesh for the computation of internal forces at nodes and energy of the material in the elements, similar to an MPM computation. However, there are major differences between the two methods, the primary one being that the Lagrangian material tracers do not transport mass and that the particle domains do not define the material interfaces. The nodal velocity solution and material density are still advected using ALE's well-established, high-order, monotonic remapping algorithms [5, 7, 4, 8, 9, 10, 11] and the material interfaces are still computed using volume-conserving first- and second-order interface reconstruction methods [12, 13]. In general, quantities associated with inertial forces are transported by ALE remapping and the quantities associated with internal forces are transported on tracers: ALE LMT is a hybrid of an ALE and MPM.

Existing ALE FEM implementations can be adapted to support ALE LMT with relative ease. The present research was performed by adapting ALEGRA, a multi-material, multi-physics, hydrodynamic ALE FEM code developed at Sandia National Laboratories [5, 14, 15]. Related work has been performed successfully by Vitali and Benson [16] for the same purpose of preserving spatial variation of material properties in ALE in order to more accurately simulate the initiation of material failure. However, their work applies non-diffuse transport only to the spatially varying random variables prescribed on the initial mesh that are then applied to material failure properties. The effective transport of spatial variability is performed by retrieving the random variable from the original mesh configuration via a mapping operation. The ALE LMT method, as described in concept above and in detail later, performs non-diffuse Lagrangian transport of not only the initial prescribed spatial variability of material properties, but also of the deformation gradient, stress tensor, and material history variables. Preservation of these quantities in ALE LMT ensures full consistency of the material state and affects the overall solution of the motion and not just the localized initial failure predicted using ALE, as in [16]. However, preserving the integrity of these additional quantities in ALE LMT (which should be a substantial improvement for problems involving damage and other extreme and localized changes in the material state) adds complexity to the method that currently results in inaccuracies (relative to standard ALE) that will require additional work to resolve (see the discussion in Section 4 of this paper).

The next section briefly reviews the governing continuum equations of motion for a deformable solid. Section 3 presents the ALE LMT method in which the discrete form of the governing equations are developed. The steps of the Lagrangian part of the computational cycle are provided, in which LMT transport of material quantities takes place, and the subsequent remapping step is outlined. ALE LMT simulation results for three problems are provided in Section 4. A simple problem of rigid body motion is used to demonstrate non-diffuse transport provided by LMT. A code verification of the ALE LMT method in ALEGRA is performed using a manufactured solution for a solid mechanics problem that incorporates geometric and material nonlinearities. The method is then applied to the problem of fragmentation of a thin ring subjected to centrifugal loading. A comparison with ALE results reveals the potential of ALE LMT for extending the range of applicability of ALE to problems of real material failure modeling using random spatial variation of material properties. Section 5 concludes and discusses future method research and development efforts.

2 Governing Continuum Equations of a Deformable Solid

Consider the deformation of a solid body in time $t \in \mathbb{R}$. Let $\Omega_0 \subset \mathbb{R}^3$ be the initial, or reference, configuration of the body at t=0 with boundary $\partial \Omega^0$. The initial position of material points are denoted as $\mathbf{X} \in \Omega_0 \cup \partial \Omega^0$. Let $\Omega \subset \mathbb{R}^3$ be the current configuration of the body at a time t>0 with boundary $\partial \Omega$. The material point locations in Ω are denoted as $\mathbf{x} \in \Omega \cup \partial \Omega$. A one to one mapping, $\mathbf{x} = \mathbf{x}(\mathbf{X}, t)$, $\mathbf{X} = \mathbf{X}(\mathbf{x}, t)$, exists between the material points positions in the initial and final configurations, and the displacement is defined as $\mathbf{u}(\mathbf{x}, t) = \mathbf{x} - \mathbf{X}$. The deformation gradient is defined as $\mathbf{F} = d\mathbf{x}/d\mathbf{X} = \nabla \mathbf{u} + \mathbf{I}$, for which ∇ denotes the gradient with respect to the current configuration, \mathbf{I} is the second order identity tensor and $J = \det \mathbf{F} > 0$. The material velocity is defined to be $\mathbf{v}(\mathbf{x}, t) = \dot{\mathbf{u}}$, where the superimposed dot denotes the material time derivative of a quantity.

The governing equations are the conservation of mass and momentum. The conservation of mass is

$$\dot{\rho} + \rho \left(\nabla \cdot \mathbf{v} \right) = 0 \quad \forall \quad \mathbf{x} \in \Omega$$
 (1)

where $\rho(\mathbf{x}, t)$ is the material density. The conservation of momentum is

$$\nabla \cdot \boldsymbol{\sigma} + \mathbf{b} = \boldsymbol{\rho} \dot{\mathbf{v}} \quad \forall \quad \mathbf{x} \in \Omega$$

where $\sigma(\mathbf{x}, t)$ is the symmetric Cauchy stress tensor and $\mathbf{b}(\mathbf{x}, t)$ is the body force per unit volume.

The initial conditions at t = 0 are

$$\mathbf{v} = \mathbf{v}^0 \quad \forall \quad \mathbf{X} \in \partial \Omega^0 \tag{3}$$

and the boundary conditions are

$$\mathbf{v} = \bar{\mathbf{v}} \qquad \forall \quad \mathbf{x} \in \partial \Omega^{\nu}$$

$$\mathbf{\tau} = \mathbf{\sigma} \cdot \mathbf{n} \quad \forall \quad \mathbf{x} \in \partial \Omega^{\tau}$$

$$(4)$$

where velocity and traction boundary conditions are applied on $\partial \Omega^{\nu}$ and $\partial \Omega^{\tau}$ respectively, with $(\partial \Omega^{\nu} \cup \partial \Omega^{\tau}) \subset \partial \Omega$, $\partial \Omega^{\nu} \cap \partial \Omega^{\tau} = \emptyset$, and where $\mathbf{n}(\mathbf{x}, t)$ is the unit normal vector on $\partial \Omega$.

Material models are applied for all $\mathbf{x} \in (\Omega \cup \partial \Omega)$. The complete constitutive model, which provides the full stress tensor, is expressed symbolically as follows:

$$\sigma = f(\mathbf{F}, \mathbb{I}) \tag{5}$$

where the quantity \mathbb{I} represents a set of history variables.

Equations (1) - (5) represent a complete set of equations for the initial boundary value problem for a deformable solid. For future reference the variational, or weak, form of the conservation of momentum in equation (2) is

$$\int_{\Omega} \rho \dot{\mathbf{v}} \cdot \mathbf{w} d\Omega = \int_{\partial \Omega^{\tau}} \tau \cdot \mathbf{w} d(\partial \Omega^{\tau}) - \int_{\Omega} \nabla \mathbf{w} : \sigma d\Omega + \int_{\Omega} \mathbf{b} \cdot \mathbf{w} d\Omega$$
 (6)

where $\mathbf{w}(\mathbf{x}, t)$ is an admissible variation of the solution for which $\mathbf{w} = \mathbf{0} \quad \forall \quad \mathbf{x} \in \partial \Omega^{\nu}$.

3 The ALE LMT Method

The basic ALE LMT method is presented in this section. The discrete governing equations are developed and the Lagrangian, remeshing, and remapping steps that comprise the ALE LMT computational cycle are summarized. For the sake of simplicity, only single-material ALE computations are considered.

3.1 Spatial Discretization for ALE LMT

A spatial discretization of an ALE LMT problem is illustrated in Figure 1 for which a typical finite element discretization is utilized. The computational domain consists of a set of elements $\{\Omega_e\}_{e=1}^{N_e}$ connected by a set of vertices, or nodes $\{\mathbf{x}_i\}_{i=1}^{N}$. The material domain, Ω (represented by the shaded region in Figure 1), is also associated with the set of discrete points, referred to as Lagrangian material tracers (LMT) $\{\mathbf{x}_t\}_{t=1}^{N_t}$. A local set of tracers $\{\mathbf{x}_t\}_{t=1}^{N_{et}} \subset \Omega_e$ is defined for each $\Omega_e \in \Omega$.

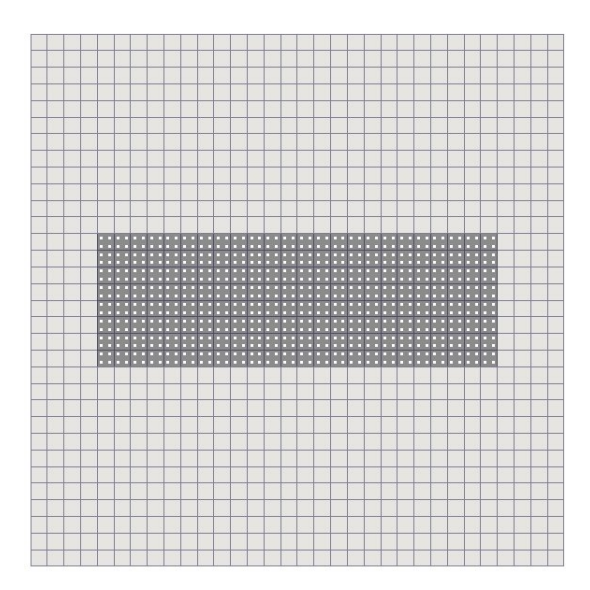


Figure 1. Spatial discretization of ALE LMT

The standard finite element method approximation used to represent the velocity field solution is

$$\mathbf{v}(\mathbf{x},t) = \sum_{i=1}^{N} \mathbf{v}_i(t) N_i(\mathbf{x})$$
 (7)

where the subscript i = 1, 2, ..., N denotes quantities at the nodes \mathbf{x}_i and the approximating "shape" functions $N_i(\mathbf{x})$ have the property that $\sum_{i=1}^{N} N_i(\mathbf{x}) = 1$. The approximation in equation (7) is also

applied to the solution variation $\mathbf{w}(\mathbf{x},t)$, and both expressions are substituted into (6). The final result is

$$m_i \dot{\mathbf{v}}_i = \mathbf{f}_i^{int} + \mathbf{f}_i^{ext} \tag{8}$$

Equation (8) is the spatially discrete conservation of momentum for which the nodal internal forces \mathbf{f}_{i}^{int} are

$$\mathbf{f}_{i}^{int} = -\int_{\Omega} \boldsymbol{\sigma} \cdot \nabla N_{i}(\mathbf{x}) d\Omega \tag{9}$$

the external nodal forces are

$$\mathbf{f}_{i}^{ext} = \int_{\Omega} \mathbf{b} N_{i}(\mathbf{x}) d\Omega + \int_{\partial \Omega^{\tau}} \tau N_{i}(\mathbf{x}) d(\partial \Omega^{\tau})$$
 (10)

and the lumped nodal mass m_i is

$$m_i = \int_{\Omega} \rho N_i(\mathbf{x}) d\Omega \tag{11}$$

The integral for \mathbf{f}_i^{int} in (9) is evaluated numerically over all Ω_e in the support of $N_i(\mathbf{x})$. The contribution from Ω_e is

$$\int_{\Omega_e} \boldsymbol{\sigma} \cdot \nabla N_i(\mathbf{x}) d\Omega_e \approx \sum_{n=1}^{n^{int}} \omega_n \bar{\boldsymbol{\sigma}}_e \cdot \nabla N_i(\boldsymbol{\psi}_n) \mathbb{J}(\boldsymbol{\psi}_n)$$
(12)

where the subscript $n = 1, 2, ..., n^{int}$ denotes a quantity evaluated at a Gaussian quadrature point ψ_n (local element coordinates), ω_n is the weight and \mathbb{J} is the Jacobian of transformation for the element computed from the following isoparametric representation of the element geometry

$$\mathbf{x}_n = \sum_{i=1}^N \mathbf{x}_i N_i(\boldsymbol{\psi}_n) \tag{13}$$

The quantity $\bar{\sigma}_e$ in equation (12) is defined as the aggregated element stress computed from the tracers $\{\mathbf{x}_t\}_{t=1}^{N_{et}} \subset \Omega_e$

$$\bar{\sigma}_e = \sum_{\mathbf{x}_t \in \Omega_e} T_e(\mathbf{x}_t) \sigma_{\mathbf{x}_t} \tag{14}$$

where the weighting function T_e determines the influence of each tracer on an element. For proof of concept in this paper the tracer weighting function is simply defined as

$$T_e(\mathbf{x}) = \frac{1}{N_{et}} \tag{15}$$

which has the undesirable properties that individual element stresses jump each time a tracer crosses an element boundary, and that the volume of the material in the element represented by the tracer is not accounted for. These properties are the likely cause of the inaccuracies relative to standard ALE highlighted during code verification in section 4.2 and could likely be mitigated using the concepts developed by Sadeghirad et.al. [17] for the MPM method.

In general, the quantity $\bar{\beta}_e$ denotes the aggregation of a quantity β onto Ω_e from the values of $\{\beta_t\}_{t=1}^{N_{et}}$ corresponding to the set of tracers $\{\mathbf{x}_t\}_{t=1}^{N_{et}} \subset \Omega_e$. The ALE LMT solution method requires

the aggregation operation for the quantities associated with nodal internal forces that include σ , \mathbf{F} , as well as \mathbb{I} , which is used for the so-called "background material", discussed below.

The ALE LMT method was intended to be used for shock and multi-physics problems where materials may expand significantly and transition from solid to liquid and gaseous phases. It would be possible to accommodate large expansions by introducing new tracers in elements that have a material present without tracers for that material. However, creating tracers introduces additional complexity, and traditional ALE methods are proficient at handling liquids and gases, which can usually be represented by an equation of state alone. Hence, the ALE LMT method maintains the state of the materials in each element so that the material properties can be smoothly transitioned to standard ALE advection methods when no tracers are present. When no tracers are present, standard ALE methods are used to compute element quantities (instead of aggregation from tracers). The materials stored in the element are referred to as "background materials" because their properties are not used until necessary. Note that maintaining the background material requires additional storage and computation that is not leveraged in standard solid-mechanics applications with small deformations (provided a few tracers per element are used).

3.2 The Lagrangian Step

The ALE LMT computational cycle consists of two basic processes; an updated Lagrangian step and a remap (advection step). During the Lagrangian step, the discrete equations of motion are integrated over a time step Δt . Let the superscript k=1,2,... denote a quantity evaluated at a discrete time t^k , and define the time step between two discrete times as $\Delta t = t^{k+1} - t^k$. Let V_e denote the volume of element e. At the beginning of the Lagrangian step the quantities, \mathbf{x}_i^k , $\mathbf{v}_i^{k-\frac{1}{2}}$, V_e^k , ρ_e^k , \mathbf{F}^k , σ_t^k and \mathbb{I}_t^k are available. These quantities are updated to \mathbf{x}_i^{k+1} , $\mathbf{v}_i^{k+\frac{1}{2}}$, V_e^{k+1} , ρ_e^{k+1} , \mathbf{F}^{k+1} , σ_t^{k+1} and \mathbb{I}_t^{k+1} at the end of the Lagrangian step using a central difference or predictor-corrector (midpoint) [18] time integration scheme. The following computations outline the basic Lagrangian step used in ALEGRA [19]. For the sake of brevity some details of the algorithm are excluded which include incorporation of artificial viscosity, hourglass control and the treatment of multi-material elements [20].

1. Compute the lumped mass matrix:

$$m_i^k = \sum_{\Omega_e \in \Omega} \int_{\Omega_e} \rho_e^k N_i(\mathbf{x}) d\Omega_e \tag{16}$$

2. Perform the aggregation of tracer stress and history variables on elements (the latter to preserve the background material):

$$\bar{\sigma}_e^k = \sum_{\mathbf{x}_t \in \Omega_e} T_e(\mathbf{x}_t) \sigma_t^k, \quad \bar{\mathbb{I}}_e^k = \sum_{\mathbf{x}_t \in \Omega_e} T_e(\mathbf{x}_t) \mathbb{I}_t^k$$
(17)

3. Compute the nodal internal forces:

$$\mathbf{f}_{i}^{int,k} = \sum_{\Omega_{e} \in \Omega} \int_{\Omega_{e}} \bar{\sigma}_{e}^{k} \cdot \nabla N_{i}(\mathbf{x}) d\Omega_{e}$$
(18)

4. Compute the nodal external forces:

$$\mathbf{f}_{i}^{ext,k} = \sum_{\Omega_{e} \in \Omega} \int_{\Omega_{e}} \mathbf{b}^{k} N_{i}(\mathbf{x}) d\Omega_{e} + \int_{\partial \Omega^{\tau}} \tau^{k} N_{i}(\mathbf{x}) d(\partial \Omega^{\tau})$$
(19)

5. Compute the nodal accelerations:

$$\dot{\mathbf{v}}_i^k = \frac{1}{m_i^k} \left(\mathbf{f}_i^{int,k} + \mathbf{f}_i^{ext,k} \right) \tag{20}$$

6. Update the nodal velocities:

$$\mathbf{v}_{i}^{k+\frac{1}{2}} = \mathbf{v}_{i}^{k-\frac{1}{2}} + \Delta t \dot{\mathbf{v}}_{i}^{k} \tag{21}$$

7. Apply velocity boundary conditions:

$$\mathbf{v}_{i}^{k+\frac{1}{2}} = \bar{\mathbf{v}}^{k} \quad \forall \quad \mathbf{x}_{i}^{k} \in \partial \Omega^{v}$$
 (22)

8. Update the nodal positions:

$$\mathbf{x}_i^{k+1} = \mathbf{x}_i^k + \Delta t \mathbf{v}_i^{k+\frac{1}{2}} \tag{23}$$

9. Evaluate the velocity gradient $\nabla \mathbf{v}_e^{k+1}$.

$$\nabla \mathbf{v}_e^{k+1} = \sum_{i=1}^N \left(\mathbf{v}_i^{k+\frac{1}{2}} \otimes N_i(\mathbf{x}_e) \right)$$
 (24)

10. Update deformation gradient on Lagrangian material tracers \mathbf{F}_{t}^{k+1} :

$$\mathbf{F}_{t}^{k+1} = \mathbf{F}_{t}^{k} \cdot \left(\mathbf{I} + \Delta t \, \nabla \mathbf{v}_{e}^{k+1} \right) \quad \forall \quad \mathbf{x}_{t} \in \Omega_{e}$$
 (25)

11. Update element volumes:

$$V_e^{k+1} = \det\left(\mathbf{I} + \Delta t \,\nabla \mathbf{v}_e^{k+1}\right) V_e^k \tag{26}$$

12. Update element densities:

$$\rho_e^{k+1} = \rho_e^k \frac{V_e^k}{V_e^{k+1}} \tag{27}$$

13. Perform the aggregation of tracer deformation gradient on elements:

$$\bar{\mathbf{F}}_e^k = \sum_{\mathbf{x}_t \in \Omega_e} T_e(\mathbf{x}_t) \mathbf{F}_t^k \tag{28}$$

14. Evaluate complete constitutive model to update stress and history variables on tracers (and perform the same operation to update the element quantities using the aggregated quantities $\bar{\mathbf{F}}_e^{k+1}$, $\bar{\sigma}_e^k$, and $\bar{\mathbb{I}}_e^k$):

$$\{\boldsymbol{\sigma}_t, \mathbb{I}_t\}^{k+1} = f\left(\mathbf{F}_t^{k+1}, \boldsymbol{\sigma}_t^k, \mathbb{I}_t^k\right) \quad \forall \quad \mathbf{x}_t \in \Omega_e$$
 (29)

15. Update tracer positions:

$$\mathbf{x}_{t}^{k+1} = \mathbf{x}_{t}^{k} + \Delta t \sum_{i=1}^{N} \mathbf{v}_{i}^{k+\frac{1}{2}} N_{i}(\mathbf{x}_{t}^{k})$$
(30)

Transport of the element quantities, σ , \mathbb{I} and \mathbf{F} on Lagrangian material tracers accomplished during the Lagrangian step of the cycle and their values computed for the k+1 time step. The ALE computational cycle requires that the remaining material quantities be transported from the mesh defined by the updated mesh node positions $\{\mathbf{x}_i^{k+1}\}_{i=1}^N$ to a target mesh \mathbb{M} defined by $\{\mathbf{x}_i^{\mathbb{M}}\}_{i=1}^N$. For the Eulerian representation $\mathbf{x}_i^{\mathbb{M}} = \mathbf{x}_i^0$.

3.3 The Remap Step

The Lagrangian step of the ALE LMT computational cycle is followed by a remeshing step and then a remapping step. During the remap process of an ALE computational cycle the updated variables at time t^{k+1} are mapped back to the target mesh elements defined by the node positions $\mathbf{x}_i^{\mathbb{M}} \in \Omega^k$. All quantities, except for those associated with Lagrangian material tracers (stress, deformation gradient, and history variables), are remapped (in this implementation, the aggregated material quantities are remapped to ensure a smooth transition when all tracers for a material are transported out of an element). A complete description of the basic ALE remapping algorithm is provided by Peery and Carroll [5]. The advection transport equation is provided by the following conservation law for a scalar quantity $\boldsymbol{\omega}$:

$$\frac{\partial \boldsymbol{\omega}}{\partial t} + \nabla \cdot (\boldsymbol{\omega} \mathbf{v}) = 0 \tag{31}$$

The use of advection transport to remap element-centered quantities from the deformed Lagrangian mesh to the stationary spatial mesh relies on an arrangement of elements that is locally rectangular in two dimensions (see Figure 2). The elements are four node quadrilateral or eight node hexahedral for two and three dimensions respectively. Element centered variables that are remapped after the Lagrangian step in a standard ALE computation include ρ_e^{k+1} , σ_e^{k+1} , \mathbf{F}_e^{k+1} , and \mathbb{I}_e^{k+1} . The advected quantities at the end of the remap step are denoted by $\hat{\rho}_e^{k+1}$, $\hat{\sigma}_e^{k+1}$, \mathbf{F}_e^{k+1} and \mathbb{I}_e^{k+1} .

The remapping computation is dimensionally split into sweep directions $\alpha = 1,...,nd$, where nd is the dimension of the problem [21, 5]. Figure 3 illustrates the elements considered for a one dimensional sweep direction, $\alpha = 1$, of material in an element Ω_e . During a single sweep, volumetric fluxes are only computed across element faces that are normal to the sweep direction

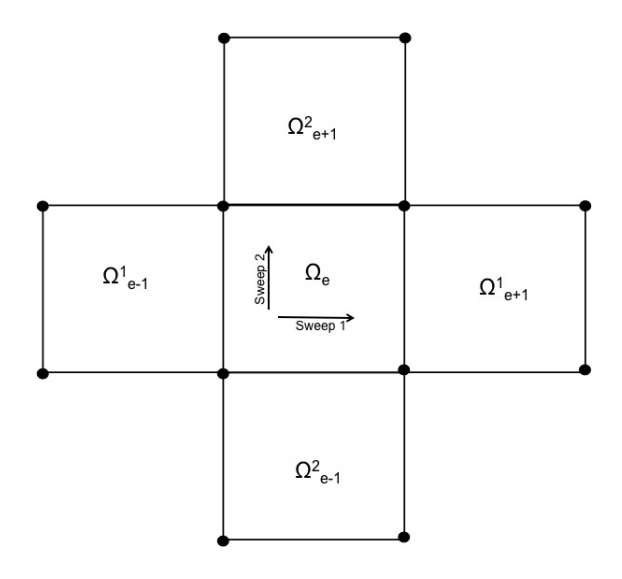


Figure 2. Local arrangement of 2D quadrilateral elements considered for remapping of element centered variables in Ω_e

after mapping to a locally rectangular coordinate system. As a result only the elements that share a face with Ω_e are considered during remap, excluding elements that share only vertices with Ω_e (corner elements). The single-sweep discretization includes coordinates for the three element centers (e-1,e,e+1) and the adjoining faces $(e-\frac{1}{2},e+\frac{1}{2})$ across which volume flux is computed. Element-centered quantities are considered to be a continuous function of volume coordinates along the sweep direction (hence the diffusion that occurs with discontinuous functions such as material damage). Although the presentation of remapping is expressed in terms of volumes and volume fluxes, it should be noted that some element-centered quantities are considered to be functions of mass coordinates along the sweep direction and are associated with mass fluxes across element faces.

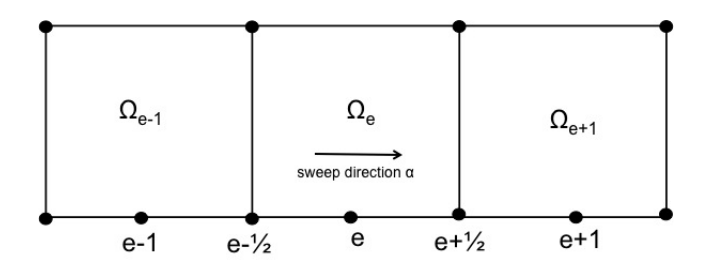


Figure 3. Discretization of a single remap sweep direction, $\alpha = 1,...,nd$, for 2D element Ω_e

The integral form of equation (31) leads to the following discrete form used to update the element-centered scalar quantity ω_e

$$\omega_e^{\alpha} = \frac{1}{V_e^{\alpha}} \left(\omega_e^{\alpha - 1} V_e^{\alpha - 1} + \tilde{\omega}_{e + \frac{1}{2}}^{\alpha} \Delta V_{e + \frac{1}{2}}^{\alpha} + \tilde{\omega}_{e - \frac{1}{2}}^{\alpha} \Delta V_{e - \frac{1}{2}}^{\alpha} \right)$$
(32)

where $\Delta V_{e\pm\frac{1}{2}}^{\alpha}$ denotes the volumetric flux of material in the one-dimensional sweep direction α , across the left $(e-\frac{1}{2})$ or right $(e+\frac{1}{2})$ faces of Ω_e for a single sweep, $V_e^0=V_e^{k+1}$, and $\omega_e^0=\omega_e^{k+1}$. Advection of ω is assumed to take place during the current time step Δt . The volume of Ω_e after a sweep in the α direction is defined as follows:

$$V_e^{\alpha} = V_e^{\alpha - 1} + \Delta V_{e + \frac{1}{2}}^{\alpha} + \Delta V_{e - \frac{1}{2}}^{\alpha}$$
(33)

The new volume of Ω_e after remap is

$$\hat{V}_{e}^{k+1} = V_{e}^{k+1} + \sum_{\alpha=1}^{nd} \left(\Delta V_{e+\frac{1}{2}}^{\alpha} + \Delta V_{e-\frac{1}{2}}^{\alpha} \right)$$
 (34)

and $\hat{\omega}_e^{k+1} = \omega_e^{nd}$. The volumetric flux across an element face for a single sweep is expressed as follows:

$$\Delta V_{e\pm\frac{1}{2}}^{\alpha} = \Delta t \int_{\partial\Omega_{e\pm\frac{1}{2}}^{\alpha}} (\mathbf{v} \cdot \mathbf{n})_{e\pm\frac{1}{2}}^{\alpha} d\left(\partial\Omega_{e\pm\frac{1}{2}}^{\alpha}\right)$$
(35)

However, the actual computation of of $\Delta V_{e\pm\frac{1}{2}}^{\alpha}$ is accomplished by computing the volume of the element formed by the coordinates of the face at the k and k+1 time steps (see reference [5]). Figure 4 depicts these swept volumes across the four faces of a 2D quadrilateral element Ω_e which experiences a uniform volume expansion mode of deformation. Positive and negative volume fluxes correspond to material volume leaving and entering the element respectively.

The quantity, $\tilde{\omega}_{e\pm\frac{1}{2}}^{\alpha}$, in equation (32) is interpolated, in general, from expressions of ω as a function of volume coordinates along the sweep direction. Many of these functional forms exist and comprise a widely researched topic. Schemes for approximation of $\tilde{\omega}_{e\pm\frac{1}{2}}^{\alpha}$ range in complexity and provide various orders of accuracy and properties. Several schemes are available for use in the ALEGRA code. The first-order donor method is summarized in [5]. Details on the popular second-order method developed by Van Leer is provided in [7]. Second and third order accurate schemes implemented into ALEGRA can be found in [20].

The remapping scheme is intended for the transport of scalar quantities, but ambiguity arises regarding the appropriate way to apply the remapping algorithm to second-order tensor quantities, such as σ and \mathbf{F} . The present remapping algorithm operates on each tensor component, treating it as a scalar. The matter is further complicated by the restriction that $det\mathbf{F} > 0$ must be satisfied, which would result in a constrained remapping scheme for \mathbf{F} . This issue was partially addressed in [22] by remapping the components of second-order tensors \mathbf{U} and \mathbf{R} , which represent the stretch and rotation tensors respectively, that result from the polar decomposition $\mathbf{F} = \mathbf{U} \cdot \mathbf{R}$. Experience has proven that the component by component advection of σ , \mathbf{U} and \mathbf{R} provides good results for most applications.

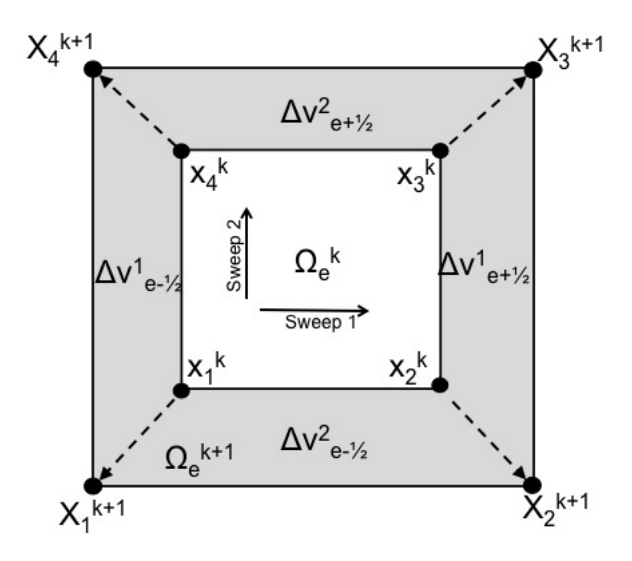


Figure 4. Illustration of swept material volumes across the faces (shaded areas) of a 2D quadrilateral element Ω_e

The remapping operation provides a transport mechanism for quantities, but is a diffusive process that tends to smear these quantities over the mesh. This characteristic is particularly disadvantageous for applications of material failure in computational solid mechanics. Discrete features such as localized strain, damage and spatial variability of strength properties are important for such applications, but are lost due to the diffusivity of advection transport. The use of Lagrangian material tracers for ALE simulations of solids eliminates these disadvantages by providing a non-diffusive transport mechanism for stress, deformation gradient and history variables. The pitfalls of component by component advection of second-order tensor quantities are also completely avoided.

4 ALE LMT Simulations

Results for three ALE LMT simulations are presented and compared to their corresponding ALE simulation results. The calculations were performed using the ALEGRA code. The first problem is a proof of concept used to demonstrate the principle of non-diffuse transport in ALE using Lagrangian tracers. The second problem is a manufactured solution utilized for verification of ALE LMT as a computational method. The last problem is an application to modeling the failure of a uniformly loaded thin ring.

4.1 Proof of Concept: Rigid Body Motion With Initial Damage

The principle of using Lagrangian material tracers for non-diffuse transport in ALE computations is demonstrated by the problem of 2D rigid body rotation of a bar about its center of mass. A comparison of ALE and ALE LMT results are provided in Figure 5. The exact motion prescribed

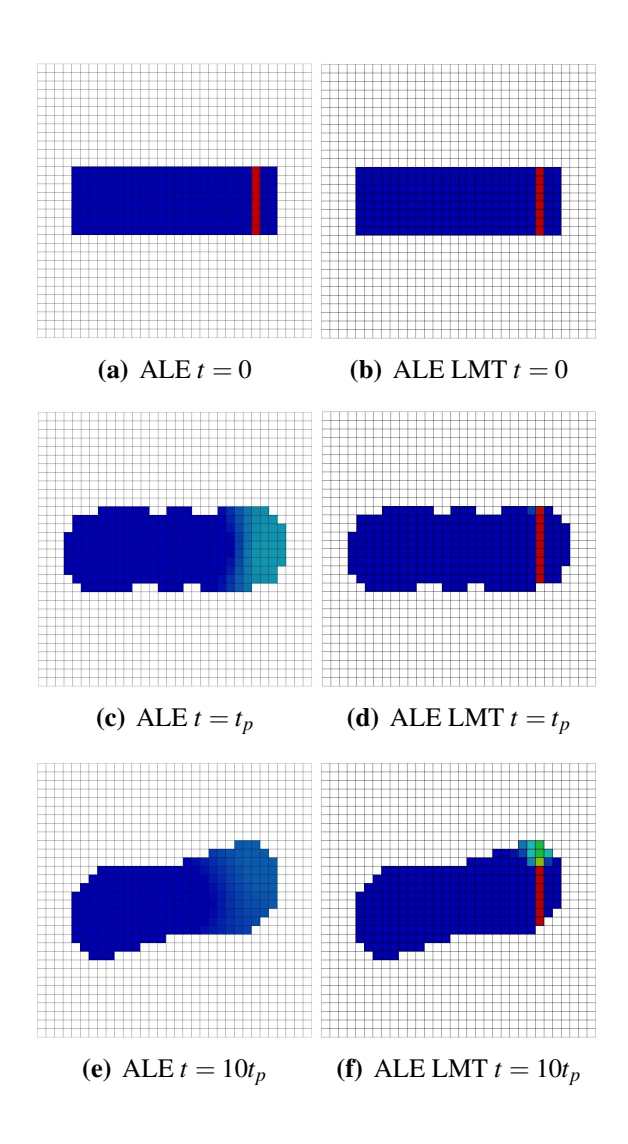


Figure 5. Bar rotation problem with prescribed initial damage: Comparison of ALE & ALE LMT damage results (blue correspond to D=0 and red corresponds to D=1)

at the nodes is

$$x_i = X_i cos(\omega t) - Y_i sin(\omega t)$$

$$y_i = Y_i cos(\omega t) + X_i sin(\omega t)$$
(36)

where (x_i, y_i) and (X_i, Y_i) are the current and reference coordinates for node i respectively, and ω is the angular speed. It is easily verified that the motion described by equation (36) is a pure rotation for which $\mathbf{F}^{-1} = \mathbf{F}^T$ and J = 1. The bar dimensions are $6\,cm \times 2\,cm$ and the rate of rotation is $\omega/(2\pi) = 100\,Hz$ corresponding to a rotational period of $t_p = 0.01\,s$. The spatial domain is discretized into $0.25\,cm \times 0.25\,cm$ four node quadrilateral elements. The elements in the material domain initially contain 4 tracer points evenly spaced along the element edges (see Figure 1). The constitutive model governing the material response is arbitrarily chosen to be the Johnson Cook fracture model [23]. The damage variable, D, plotted on the initial configurations in Figures 5a and b, is initially prescribed to a value of 1 in a local region at the right side of the bar. Since the motion given in equation (36) is purely rotational, stress does not develop in the bar preventing the accumulation of further damage.

The motion is applied, and after a single revolution the local damage pattern has been unphysically smeared over half the bar by the ALE simulation while the damage pattern has been maintained by the ALE LMT computation (Figure 5c and d). After ten revolutions the ALE LMT method has maintained the original damage pattern for the most part, however the some smearing of the damage is observed (Figure 5f).

Since the motion of the bar is completely rigid, computational results reflect only the transport of material quantities provided by either the remap algorithm of Section 3.3 or the motion of the tracers. Currently, the ALEGRA code allows transport of σ , \mathbf{F} and \mathbb{I} (which includes D) by both remapping and tracer motion during the ALE LMT computation, and the aggregation of these quantities from tracers to the elements overwrites the remapping result. However, if remapping occurs in an element where there are no tracers, the results for σ , \mathbf{F} and \mathbb{I} reflect only remap transport and are susceptible to diffusion. This case is illustrated in Figure 6 which displays the final configuration of the ALE LMT result (Figure 5f) with the tracers superimposed. It is immediately apparent that smearing of D occurs in regions where there are no tracers.

One important computational consideration for ALE LMT is the presence of two different transport mechanisms for material quantities, advection and Lagrangian tracer motion. These mechanisms are very different. Remapping is essentially an averaging of quantities in neighboring cells weighted by the flux of material through the cell faces. LMT transport is based on averaging of tracer quantities in a cell that move according to the nodal velocity solution computed during the Lagrangian step. There is no reason to expect that the motion produced by these two algorithms will be identical. As a consequence, the situation of asynchronous transport of the same material variable, depicted in Figure 6, can eventually occur. However, it should be noted that the result displayed is after 350,000 computational cycles. It should be possible to better synchronize the transport mechanisms, but this is a topic for further research.

4.2 Code Verification: Generalized Vortex Manufactured Solution

Code verification of the ALE LMT method is provided by the method of manufactured solutions (MMS) [24]. The manufactured solution for the so called 2D generalized vortex problem, developed by Kamojjala et. al. [25] for verification of the convected particle domain interpola-

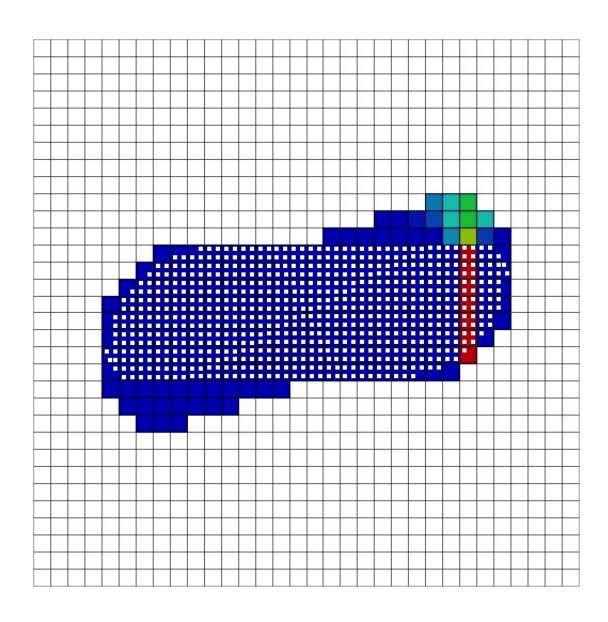


Figure 6. Bar rotation problem with prescribed initial damage at $t = 10t_p$ with Lagrangian material tracers displayed

tion (CPDI) method [17], is utilized due to it's straightforward applicability to particle-in-cell approaches. The dynamic solid mechanics problem involves a non-trivial deformation field that incorporates geometric and material nonlinearities, but does not require the enforcement of velocity or traction boundary conditions.

The initial configuration of the generalized vortex problem is depicted in Figure 7 as a twodimensional annulus of hyperelastic solid material with inner radius $R_a = 0.75 \, m$ and outer radius $R_b = 1.25 \, m$. The position of a material point **X** in the initial configuration is expressed in terms of cylindrical coordinates (R, Θ) corresponding to the orthonormal basis vectors $\{\mathbf{E}_R, \mathbf{E}_\Theta\}$. The prescribed motion is

$$\mathbf{x}(\mathbf{X},t) = R\cos(\Theta + \alpha)\mathbf{E}_x + R\sin(\Theta + \alpha)\mathbf{E}_y$$
(37)

where

$$\alpha(R,t) = g(t)h(R) \tag{38}$$

and

$$h(R) = (16(R-1)^2 - 1)^2 \quad g(t) = \frac{1}{2}(1 - \cos(2\pi t))$$
(39)

The motion described by equations (37) - (90) is simple shear with a superimposed rotation. The energy function form for the hyperelastic material model is

$$\Psi(\mathbf{F}) = \frac{\mu}{2} \left(\mathbf{F} : \mathbf{F}^T - 2 \right) - \mu \ln(J) + \frac{\lambda}{2} (\ln(J))^2$$
(40)

where $\lambda = 577 Pa$ and $\mu = 385 Pa$ are the Lame material constants, which correspond to a Young's modulus of E = 1000 Pa and a Poisson's ratio of v = 0.3. The Cauchy stress σ is obtained from

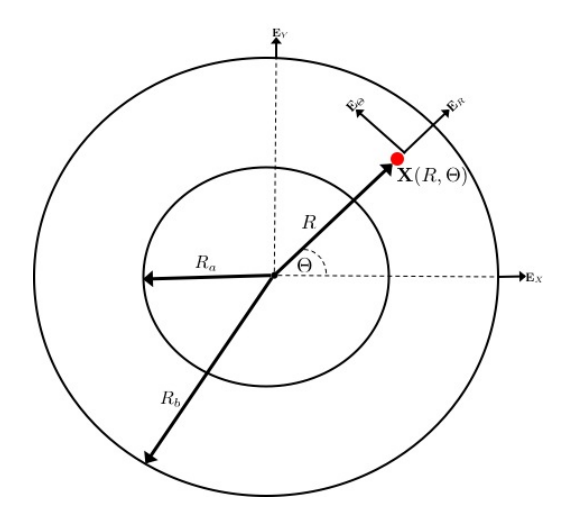


Figure 7. Initial configuration of generalized vortex problem

equation (40) as follows:

$$\sigma = J^{-1} \frac{d\Psi}{d\mathbf{F}} \cdot \mathbf{F}^T \tag{41}$$

The basic MMS approach is employed in order to obtain a body force function $\mathbf{b}(\mathbf{X},t) = b_r \mathbf{E}_r + b_\theta \mathbf{E}_\theta$, for which the deformed angular coordinates, r = R and $\theta = \Theta + \alpha(R,t)$, of a material point are associated with the deformed basis vectors $\{\mathbf{E}_r, \mathbf{E}_\theta\}$. Equations (37)-(41) are combined with the conservation of momentum in equation (2) and the relationships, $\mathbf{v} = \dot{\mathbf{x}}$ and $\mathbf{F} = d\mathbf{x}/d\mathbf{X}$. Details of the MMS analysis for the generalized vortex problem are provided in Appendix A. The final results for the components of $\mathbf{b}(\mathbf{X},t)$ are

$$b_{r} = -\pi^{2} \sin^{2}(2\pi t) R \left(16(R-1)^{2} - 1\right)^{4} + \frac{\mu}{4\rho_{0}} \left(1 - \cos(2\pi t)\right)^{2} R \left(1024(R-1)^{3} - 64(R-1)\right)^{2}$$

$$b_{\theta} = 2\pi^{2} \cos(2\pi t) R \left(16(R-1)^{2} - 1\right)^{2} - \frac{\mu}{2\rho_{0}} \left(1 - \cos(2\pi t)\right) 64 \left(96R^{3} - 240R^{2} + 188R - 45\right)$$

$$(43)$$

where the initial mass density of the material is $\rho_0 = 1000 kg/m^3$. The resulting body force function is used to drive the simulation, and the motion generated should be that of equation (37). It is easily verified that the resulting velocity solution is

$$\mathbf{v}(\mathbf{X},t) = (\pi R(16(R-1)^2 - 1)^2 \sin(2\pi t)) \left(-\sin(\Theta + \alpha)\mathbf{E}_x + \cos(\Theta + \alpha)\mathbf{E}_y\right)$$
(44)

Figure 8 displays the two ALE LMT discretizations considered for the generalized vortex problem. Let h denote the element size metric which is equal to the side length of a square element in the rectangular mesh (8b) and the radial cell spacing for the radial mesh (8a). The mesh resolution parameter n is used to define the element size such that $h = h_0/2^n$, where $h_0 = 0.1 m$ is the smallest mesh size considered. The Lagrangian material tracer density parameter p denotes the number of uniformly spaced tracers per cell per linear dimension. The cases of n = 0, 1, 2, 3, 4, 5 and p = 0, 3, 6, 9 are considered for each discretization.

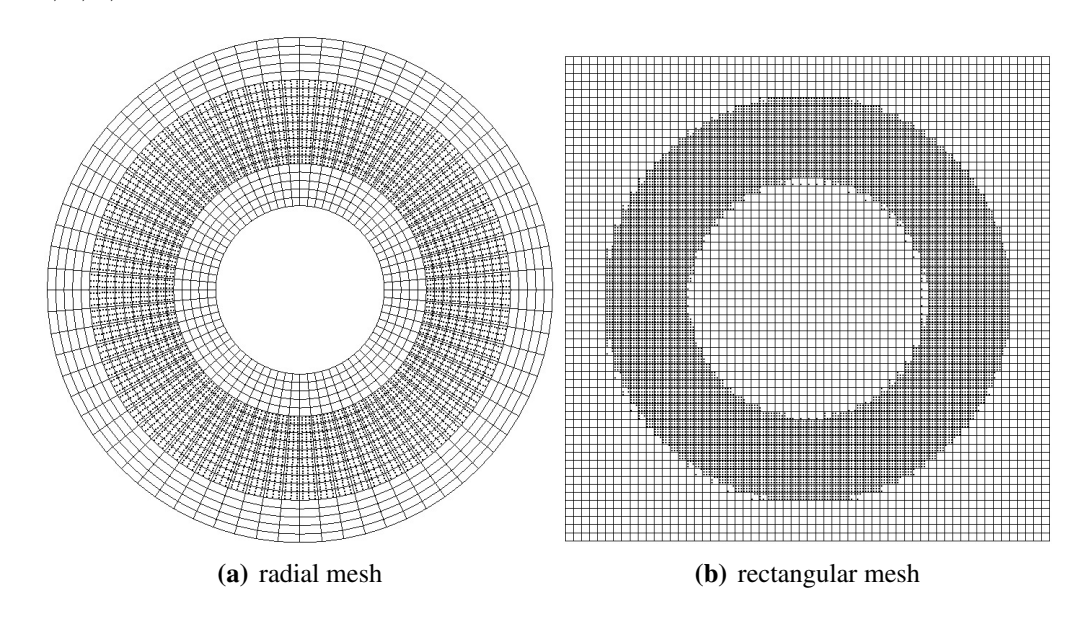


Figure 8. ALE LMT discretization of the generalized vortex problem (n = 1, p = 3).

Figures 9 and 10 display comparisons between the exact and ALE LMT numerical velocity field magnitude solutions at t = 0.25 s for the radial and rectangular meshes respectively. The exact solution is obtained by prescribing the exact velocity solution of equation (44) at nodes and the numerical ALE LMT solution is obtained by prescribing the MMS body force function result in equations (42) and (43). Sets of diagnostic Lagrangian material tracers are superimposed on the plots in order to illustrate the deformation of material. The array of radial lines placed at various angular positions at t = 0 is deformed substantially by t = 0.25 s. At this time it easily verified from equations (38) and(44) that the maximum angular displacement and velocity magnitude are $\alpha = 28.7^{\circ}$ and $\|\mathbf{v}\| = \pi m/s$ respectively for radial position R = 1 m. Exact and numerical solutions agree well by visual comparison for both radial and rectangular mesh types. A region non-zero velocity outside the material domain is noticeable in the ALE LMT results for the rectangular mesh but is absent from the radial mesh results. This is most likely attributed to the nature of the advection transport of the velocity field, which is based on flux of material in the normal direction to the cell faces. Since the circumferential mesh lines in the radial mesh are aligned with the motion of the material, a radial mesh is generally expected to provide a better result than that of a rectangular grid of the same resolution.

Error analysis of the ALE LMT nodal velocity solution at t = 0.25 s for various tracer densities are displayed in Figures 9 and 10 for the radial and rectangular meshes respectively. Convergence is achieved for both cases using the L_2 error norm, which is computed with respect to the exact velocity solution. Use of a radial mesh over a rectangular mesh generally results in a higher rate of

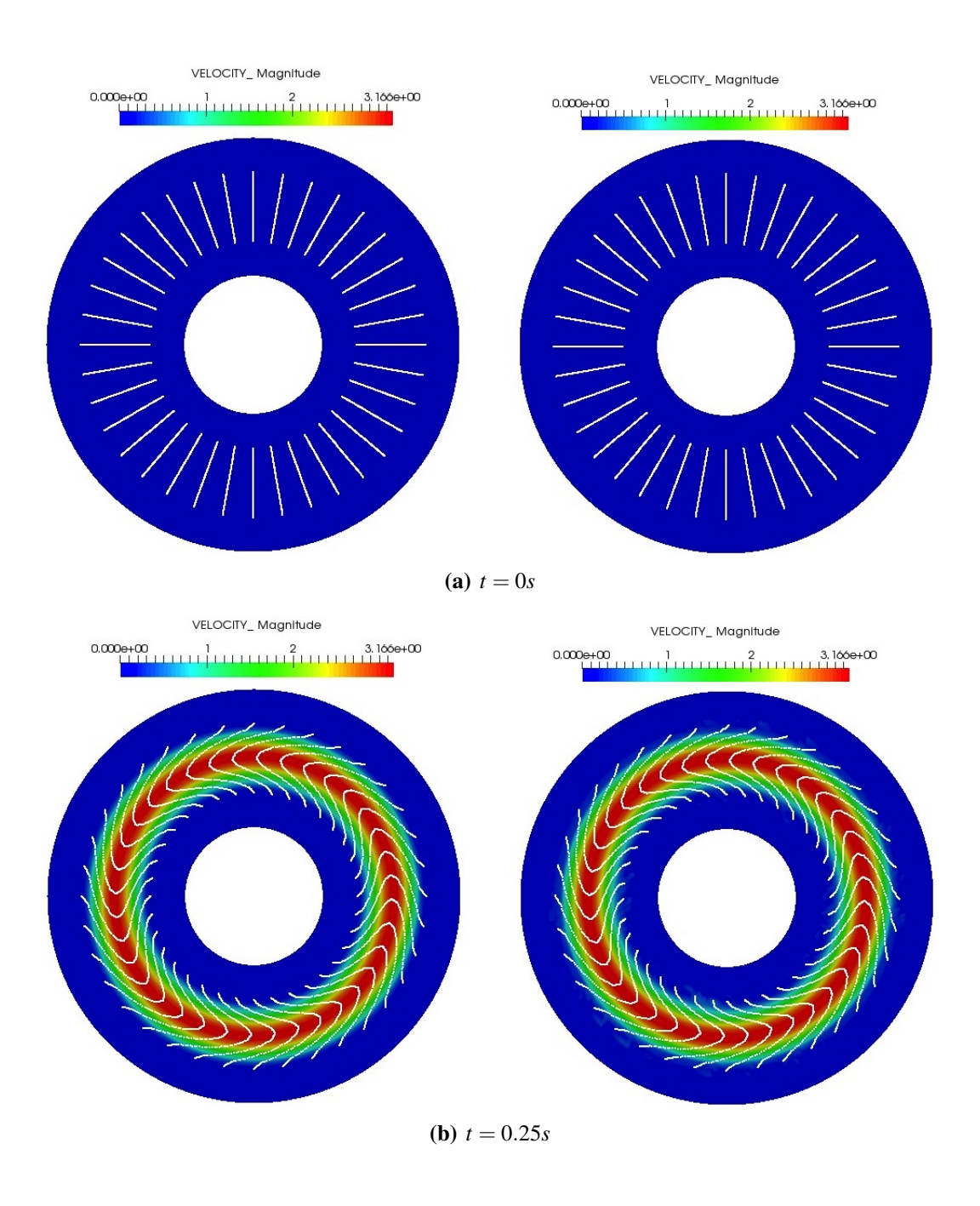


Figure 9. Comparison between the exact (left) and ALE LMT (right) velocity magnitude solutions for the generalized vortex problem with a radial mesh (n = 1, p = 3).

convergence for this problem which agrees well with that of the standard ALE case of p=0 (no tracers). ALE LMT error results for a rectangular grid result in a slower convergence rate than that of standard ALE. Particle density has no apparent effect on convergence rate for either mesh type.

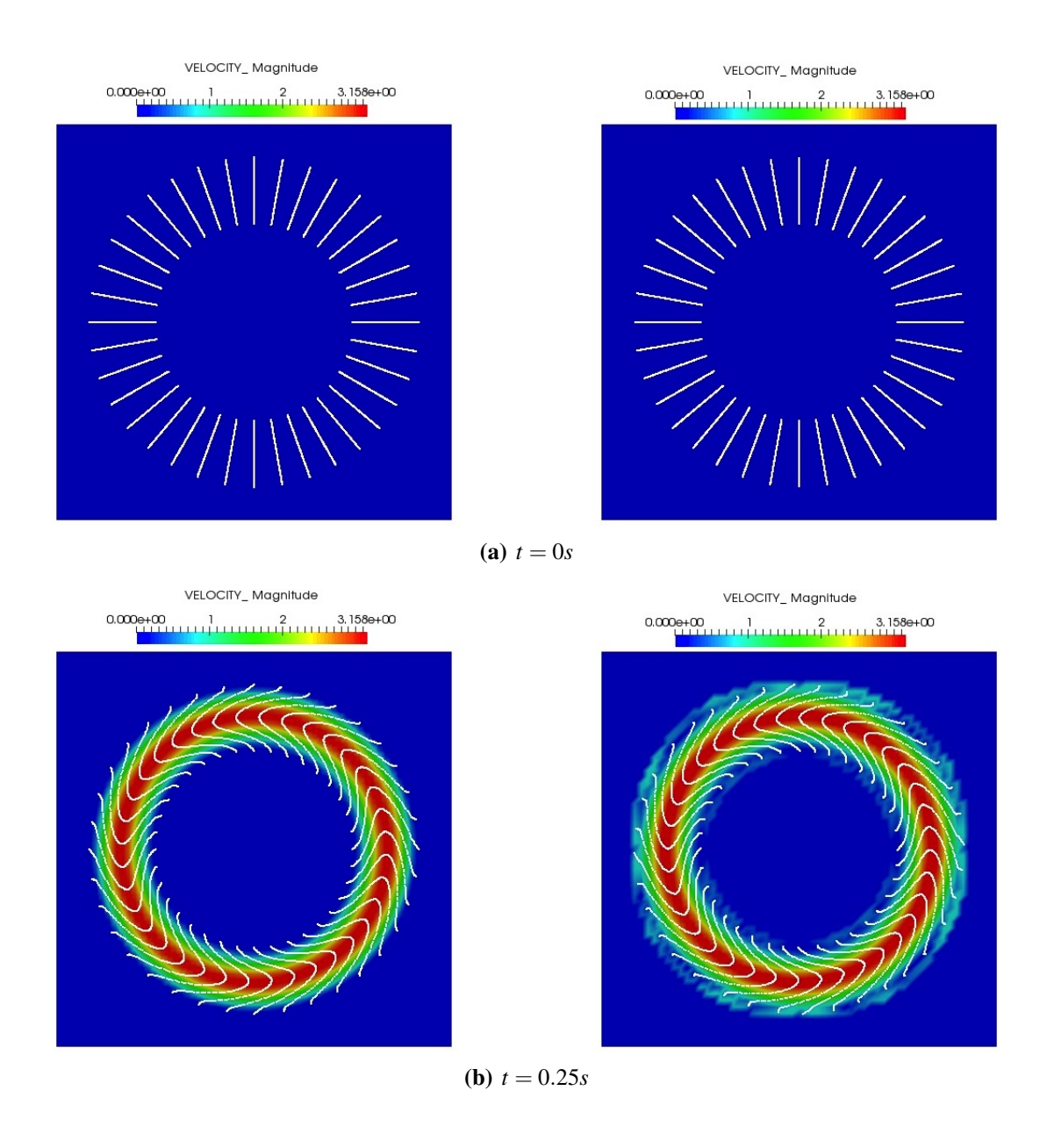


Figure 10. Comparison between the exact (left) and ALE LMT (right) velocity magnitude solutions for the generalized vortex problem with a rectangular mesh (n = 1, p = 3).

There is no fundamental reason ALE LMT should be less accurate than standard ALE. It is most likely that noise is introduced in the solution when tracers cross element boundaries. The very basic weighting function T_e introduced in equation (14) is a likely culprit. However, the ALE LMT method preserves information that is critical for the integrity of simulations involving damage. This significant improvement is demonstrated below.

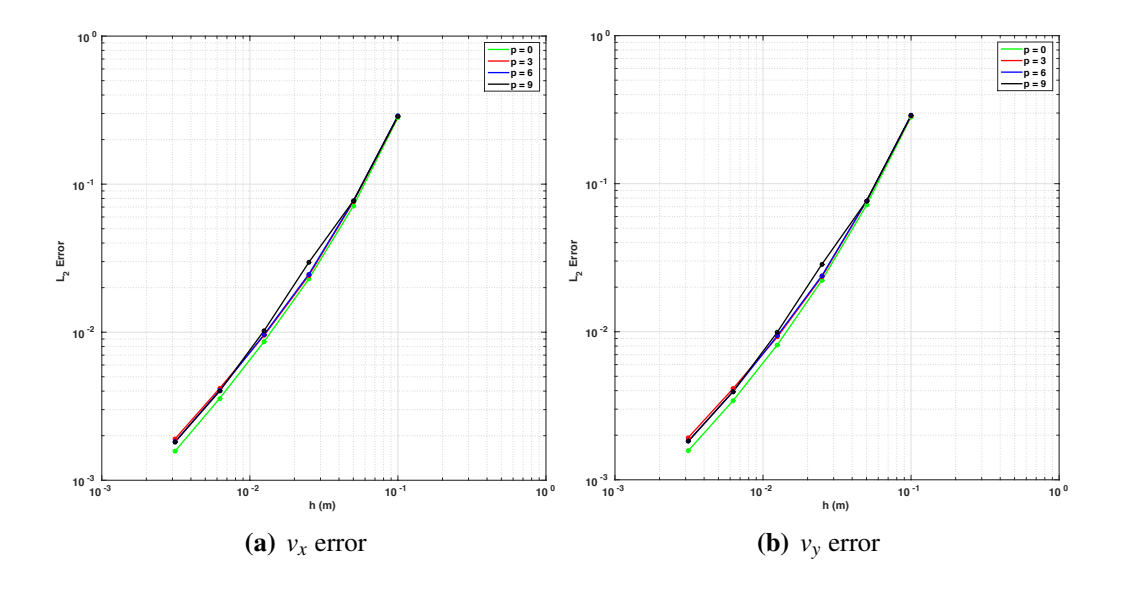


Figure 11. ALE LMT velocity solution error at t = 0.25 s for radial mesh.

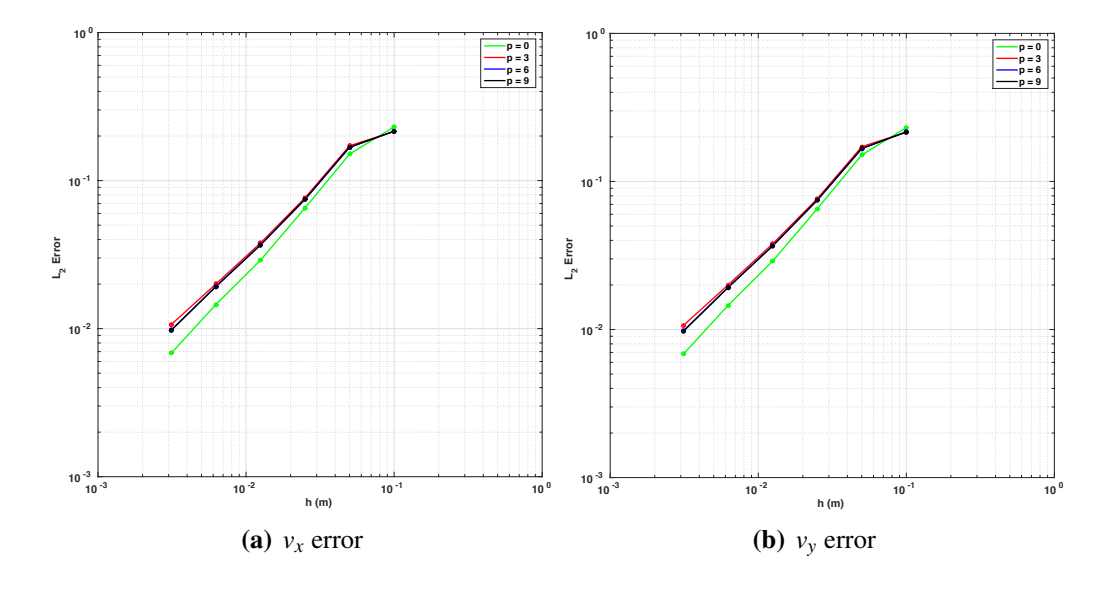


Figure 12. ALE LMT velocity solution error at t = 0.25 s for rectangular mesh.

4.3 Application: Simulation of a Rotating and Expanding Ring

The ALE LMT method is applied to the problem of the fragmentation of an expanding ring subjected to centrifugal loading. The simulations are based on experiments performed by Benson and Grady [26], in which uniform tensile load is applied to the ring using an electromagnetic field. The thin aluminum 1100-0 ring has an outer diameter of 32mm and $1mm \times 1mm$ square cross section. Experimental results show that material failure of the ring due to circumferential tension is preceded by ductile necking of the ring cross section which are localized at relatively even spaced locations along the ring's circumference.

The 2D Eulerian simulations of the expanding ring problem follow closely from the 3D Lagrangian ALE simulations performed by Bishop and Strack [1] who applied a constant pressure to the inner radius of the ring. Consider a 2D polar coordinate system with coordinates (r, θ) . The radially constructed Eulerian mesh of 16,920 quadrilateral finite elements, displayed in Figure 13, corresponds to the lowest resolution mesh used in [1] with $\Delta r = 0.25mm$. The origin is located at r = 0. The inner and outer radius of the mesh are 30.75mm and 42mm respectively.

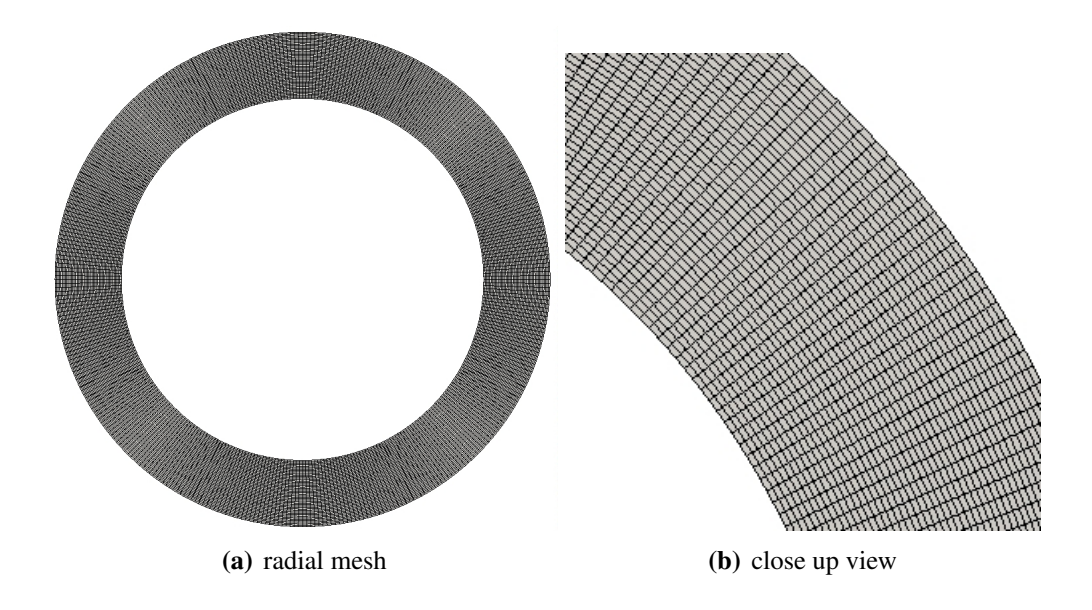


Figure 13. Eulerian mesh of cells for expanding ring problems: 16,920 cells

The ring material is modeled using the isothermal, rate-independent form of the Johnson-Cook isotropic plasticity model [28], for which the corresponding hardening function is

$$\bar{\sigma} = \sigma_{y} + H\varepsilon_{p}^{n} \tag{45}$$

where $\bar{\sigma}$ is the Von Mises stress, ε_p is the equivalent plastic strain history variable, σ_y is the initial yield stress, H is the hardening modulus and n is the hardening exponent.

The localized failure of a geometrically uniform structure subjected to spatially uniform loading is attributed to inhomogeneity in the material. In order to capture this feature of failure of real materials, a statistical approach is utilized, for which the aleatory uncertainty (uncertainty in spatial variation) and size effect of σ_y are accounted for (see [1] and [27]). The value of σ_y is taken from a Weibull probability distribution function with the following form:

$$\sigma_{y} = \bar{\sigma}_{y} \left(\frac{\bar{V}}{V} \frac{lnR}{ln\frac{1}{2}} \right)^{\frac{1}{m}} \tag{46}$$

The median value of initial yield stress for aluminum 1100 is $\bar{\sigma}_y = 80MPa$, the reference volume is $\bar{V} = 1 \, cm^3$, the Weibull modulus is m = 25, R is a random number from a uniform distribution ranging from 0 to 1 and V is the volume of a discrete finite element. An initial yield stress range of $63.2 \, MPa \le \sigma_y \le 88.2 \, MPa$ results from application of equation (46) to the discretized ring. Figure 14a displays a plot of σ_y on the initial configuration. A close up view of the spatial variation of σ_y in a ring sector is also provided in Figure 15a. The remaining material parameters in equation (37) are constant values of H = 20MPa and n = 0.34

The centrifugal loading of ring is simulated by the application of a prescribed body acceleration (external force) to the mesh nodes. The body acceleration field $\mathbf{a}(\mathbf{r},t)$ is applied to the mesh node radial positions $\mathbf{r}_i(t) = x_i \mathbf{e}_x + y_i \mathbf{e}_y$, where \mathbf{e}_x and \mathbf{e}_y are the global Cartesian unit basis vectors and (x_i, y_i) are the corresponding cartesian coordinates of a node. The body acceleration function is

$$\mathbf{a} = \alpha(t) \left(-\frac{y_i}{r} \mathbf{e}_x + \frac{x_i}{r} \mathbf{e}_y \right) \tag{47}$$

where $r = \sqrt{x_i^2 + y_i^2}$ and the angular acceleration α is

$$\alpha(t) = \alpha_1 (H(t) - H(t - t_1)) + \alpha_2 (H(t - t_p) - H(t - t_2))$$
(48)

The Heaviside function, H(x), for any argument x is defined to be

$$H(x) = \begin{cases} 1 & x \ge 0 \\ 0 & x < 0 \end{cases} \tag{49}$$

Equation (48) represents two square pulse angular accelerations functions applied at t=0 and $t=t_p$. The first pulse accelerates the ring to an angular speed of $\omega_1=5\times 10^3 \, rad/s$ and its amplitude and duration are $\alpha_1=1\times 10^8 \, rad/s^2$ and $t_1=\omega_1/\alpha_1$ respectively. The second pulse accelerates the ring to an angular speed of $\omega_2=9\times 10^3 \, rad/s$. It has an amplitude of $\alpha_2=1\times 10^9$ and is applied after the the ring has rotated one revolution at time $t_p=2\pi/\omega_1+\omega_1/(2\alpha_1)$. The duration of the second pulse is t_2-t_p , where $t_2=(\omega_2-\omega_1)/\alpha_2+t_p$.

The uniform loading of the ring is produced by the centrifugal force resulting from rotational motion. After application of the first pulse the ring is rotating at a constant angular speed of ω_1 . The resulting stress state is tension in the circumferential direction for which $0 < \sigma_{\theta\theta} < \bar{\sigma}_y$ and $\sigma_{rr} = \sigma_{r\theta} = 0$. The value of ω_1 was obtained by trail and error in order to satisfy $\sigma_{\theta\theta} < \bar{\sigma}_y$. A rapid increase in the centrifugal force is then realized by application of the second loading pulse for which $\sigma_{\theta\theta} > \bar{\sigma}_y$. The plastic response of the material causes the ring to expand radially.

Figure 14 displays comparisons of σ_y between ALE and ALE LMT simulations at three discrete times within $0 \le t \le t_p$. A pink dot is used to trace the position of a single material point in the calculations. Initially, the ring incorporates the same spatial variation of σ_y for both methods (Figure 14a). A normal ALE simulation transports the values of σ_y using a remapping algorithm while σ_y is transported by discrete points using ALE LMT. After only a quarter rotation the loss of the spatial variation of σ_y is very apparent. The two results are compared in Figure 14b after the ring completes a full revolution. The spatial variability of the σ_y remains intact when LMT is employed, but is completely absent due to diffusive advection transport of the ALE simulation. This difference is clearly observed in Figure 15.

Comparisons of ALE and ALE LMT are displayed in Figure 16. The configurations are colored according to the equivalent plastic strain, with red corresponding to $\varepsilon_p \ge 0.5$. The comparison displayed in Figure 16b clearly shows the improved performance of ALE LMT for predicting the fragmentation of the ring, which can be deduced from the necking locations on the image on the right of Figure 16b. The physically realistic development of localized deformation (necking) is only possible because the Lagrangian material tracers provide a non-diffusive transport mechanism for the spatially varied initial yield stress field. If LMT is not utilized the result is an unrealistic uniform plastic strain in the ring (left image in Figure 16b). It is important that spatial variability of strength related quantities, such as σ_y , be maintained in order to simulate failure of real materials. Uniform geometry and loading does eventually lead to localized failure as a result of the material inhomogeneity that random variation of strength properties is intended to represent. This is certainly the case of the expanding ring experiments preformed in [26].

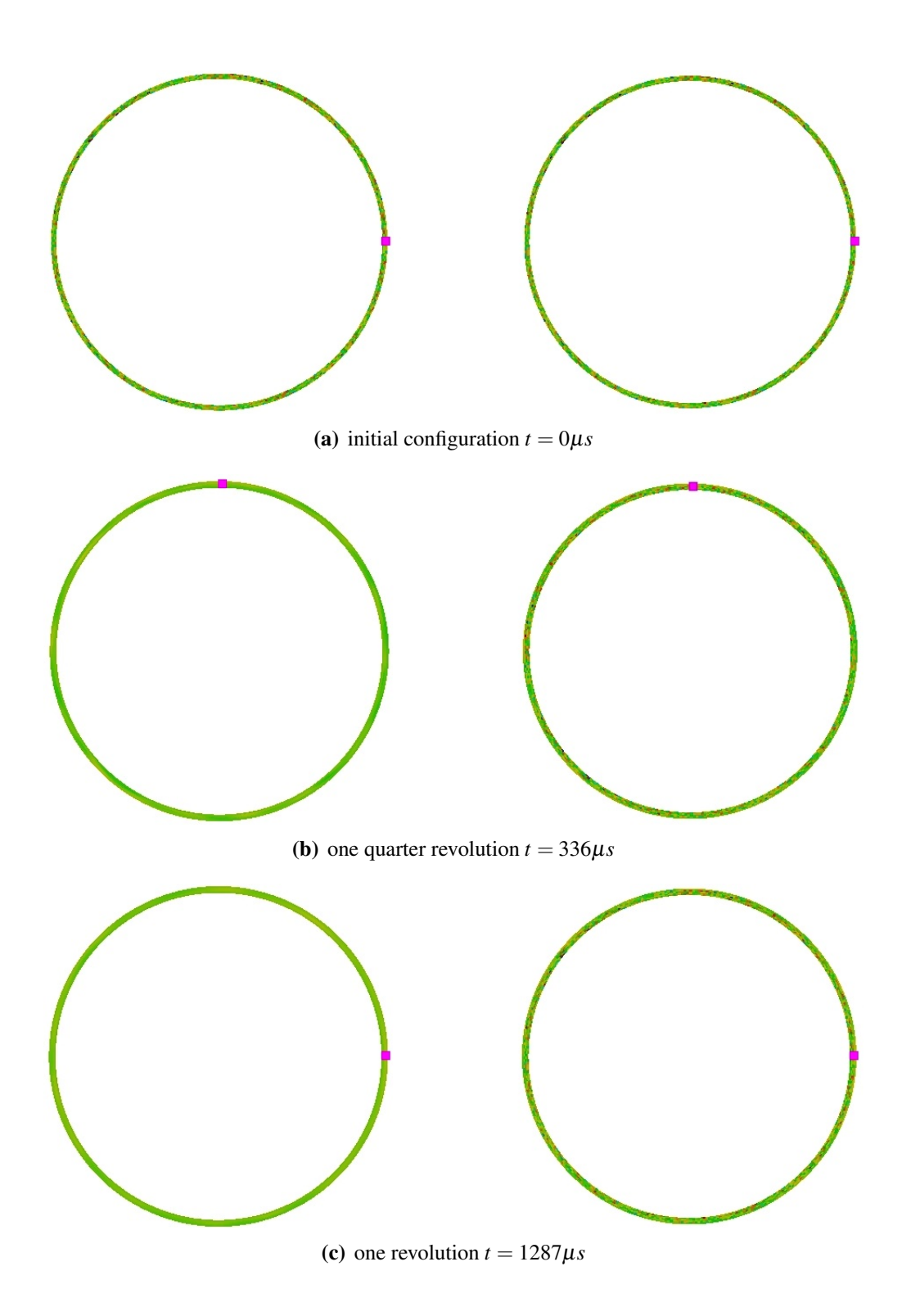


Figure 14. Comparison of spatial variation of σ_y for ALE (left) and ALE LMT (right); $63.2MPa \le \sigma_y \le 88.2MPa$

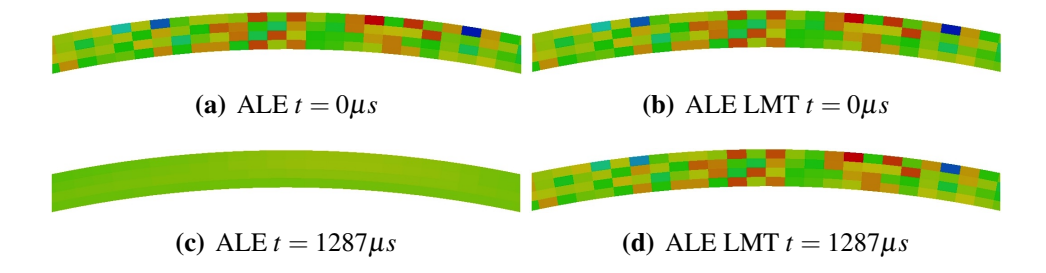


Figure 15. Close up view of a ring sector comparing spatial variation of σ_y between ALE (left) and ALE LMT (right) $63.2MPa \le \sigma_y \le 88.2MPa$

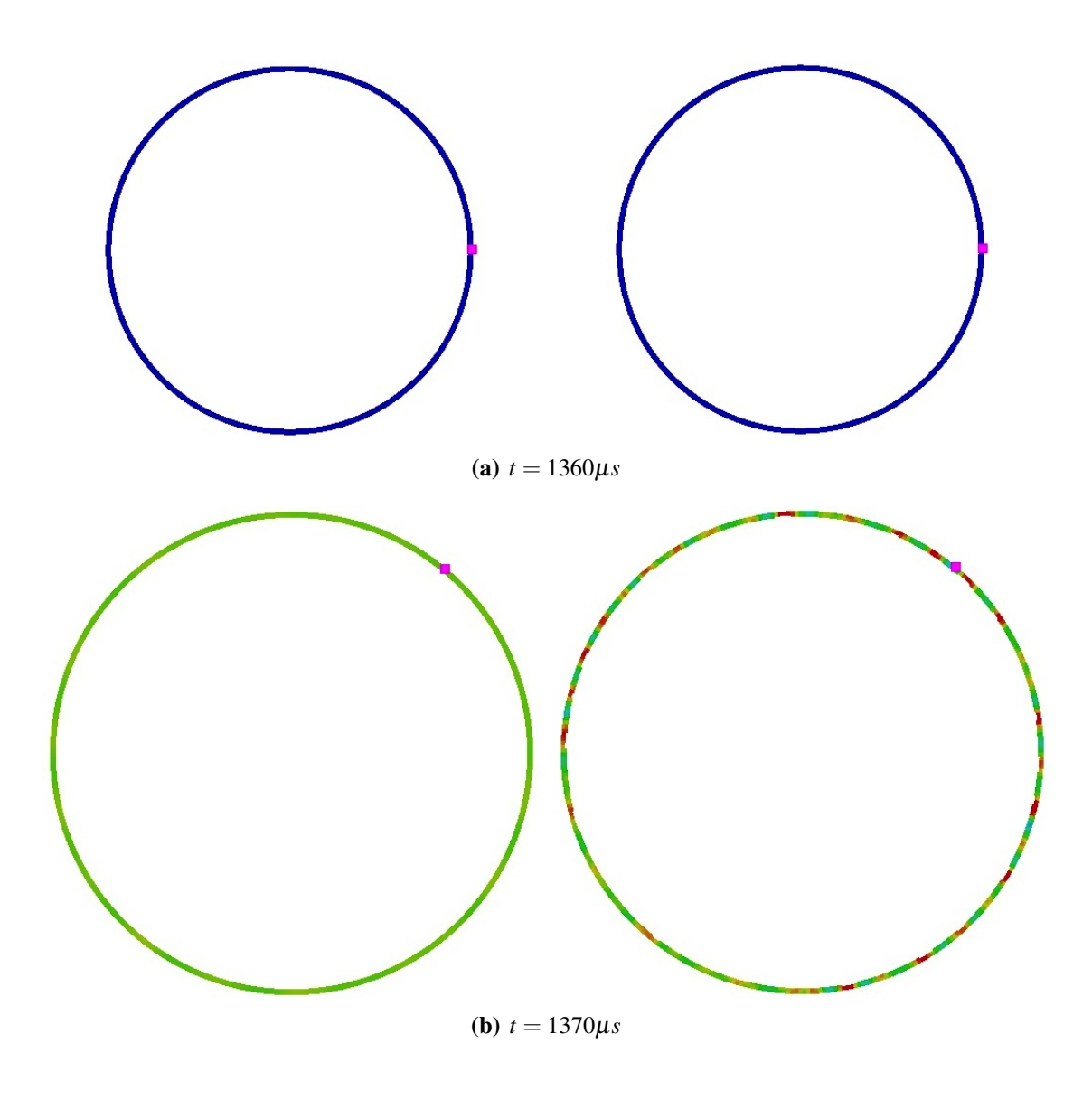


Figure 16. Comparison of equivalent plastic strain (red corresponds to $\bar{\epsilon}_p \geq 0.5$) for ALE (left) and ALE LMT (right)

5 Conclusions

The ALE LMT method has been presented and is clearly an improvement to statistical material failure modeling approaches in ALE. The hybrid ALE and particle-in-cell method uses massless points to provide a non-diffuse transport mechanism for material history variables and the deformation gradient and stress tensors. This concept is demonstrated by the preservation of a prescribed initial damage pattern on a solid subjected to rigid body motion. Verification of the ALE LMT method was performed using the generalized vortex manufactured solution, which incorporates large deformations and a non-linear material model. Use of the method for simulating a thin ring subjected to uniform centrifugal loading not only preserves the inhomogeneity in the material properties as the ring rotates, but predicts localized necking associated with realistic failure initiation. Lagrangian tracer transport of the deformation gradient and stress also eliminates the ambiguity associated with remapping these second order tensor quantities, which violates restrictions on the deformation rate or gradient.

Future ALE LMT research and development efforts are dedicated to improvement in accuracy, robustness, and performance. Methods to improve the synchronicity between motion of material quantities provided by the two transport mechanisms present in the method are currently being considered. This type of improvement plays a key role for the concept of dynamic tracer creation for material regions of large volumetric expansion where the density of tracers is too low to retain localized damage regions and destruction of tracers for material regions of large volumetric compression where the tracer density has become unnecessarily large. This type dynamic tracer population control could drastically improve the efficiency of ALE LMT. Adoption of the particle domain representation used in CPDI could also potentially improve the accuracy of the method and decrease the number of tracers necessary to discretize a domain.

A Generalized Vortex Manufactured Solution

The following development of the generalized vortex manufactured solution was first performed in [25] and is included in the present work for convenience. Consider a two-dimensional annulus with inner radius R_a and outer radius R_b depicted in Figure 7. The position of a material point in the initial configuration is expressed in terms of cylindrical coordinates (R, Θ, Z) corresponding to the orthonormal basis vectors $\{\mathbf{E}_R, \mathbf{E}_{\Theta}, \mathbf{E}_Z\}$ as follows:

$$\mathbf{X} = \mathbf{X}(R, \Theta) = R\mathbf{E}_R \tag{50}$$

The following rotational motion is prescribed for the body

$$\mathbf{x} = \mathbf{Q} \cdot \mathbf{X} \tag{51}$$

where Q is

$$\mathbf{Q} = \begin{pmatrix} \cos(\alpha) & -\sin(\alpha) & 0\\ \sin(\alpha) & \cos(\alpha) & 0\\ 0 & 0 & 1 \end{pmatrix}$$
 (52)

and

$$\alpha(R,t) = g(t)h(R) \tag{53}$$

For future reference, the following relationship is defined

$$\frac{d\mathbf{Q}}{d\alpha} = \mathbf{A} \cdot \mathbf{Q} = \mathbf{Q} \cdot \mathbf{A} \tag{54}$$

where the axial tensor A is

$$\mathbf{A} = \begin{pmatrix} 0 & -1 & 0 \\ 1 & 0 & 0 \\ 0 & 0 & 0 \end{pmatrix} \tag{55}$$

and has the following properties for any vector s.

$$\mathbf{A} \cdot \mathbf{s} = \mathbf{E}_{\mathbf{Z}} \times \mathbf{s} \quad \mathbf{s} \cdot \mathbf{A} = \mathbf{s} \times \mathbf{E}_{\mathbf{Z}} \tag{56}$$

The deformation gradient is computed from equation (51) as follows:

$$\mathbf{F} = \frac{d\mathbf{x}}{d\mathbf{X}} = \mathbf{Q} + \frac{d\mathbf{Q}}{d\mathbf{X}} \cdot \mathbf{X} \tag{57}$$

The second term in (57) is expressed using (54) and the chain rule as follows:

$$\frac{d\mathbf{Q}}{d\mathbf{X}} \cdot \mathbf{X} = \frac{d\alpha}{dR} \left(\mathbf{A} \cdot \mathbf{Q} \cdot \mathbf{X} \right) \otimes \frac{dR}{d\mathbf{X}}$$
 (58)

Equations (50), (57) and (58) are combined along with the fact that $R = \mathbf{X} \cdot \mathbf{E}_R$ and $\mathbf{E}_{\Theta} = \mathbf{A} \cdot \mathbf{E}_R$ in order to produce the following result for \mathbf{F} .

$$\mathbf{F} = \mathbf{Q} \cdot \left(\mathbf{I} + Rg \frac{dh}{dR} \mathbf{E}_{\Theta} \otimes \mathbf{E}_{R} \right) \tag{59}$$

An alternative expression for equation (59) is

$$\mathbf{F} = \mathbf{Q} \cdot \mathbf{q} \cdot \mathbf{f} \cdot \mathbf{q}^T \tag{60}$$

where

$$\mathbf{f} = \left(\mathbf{I} + Rg\frac{dh}{dR}\mathbf{E}_2 \otimes \mathbf{E}_1\right) \tag{61}$$

and

$$\mathbf{q} = \begin{pmatrix} \cos(\Theta) & -\sin(\Theta) & 0\\ \sin(\Theta) & \cos(\Theta) & 0\\ 0 & 0 & 1 \end{pmatrix}$$
 (62)

and $\{E_1, E_2, E_3\}$ is the set of standard basis vectors. Since the deformation is pure shear, it follows that

$$J = \det(\mathbf{F}) = 1 \tag{63}$$

The Lagrangian representation of the conservation of momentum is

$$\rho_0 \mathbf{a} = \nabla_0 \cdot \mathbf{P} + \rho_0 \mathbf{b} \tag{64}$$

where **a** is the acceleration, **P** is the first Piola Kirchhoff stress tensor, **b** is the body force per unit mass (body acceleration), ρ_0 is the initial material density and ∇_0 is the gradient operator with respect to the initial configuration. The objective is to obtain $\mathbf{b}(\mathbf{X},t)$ using the prescribed motion in equation (51), the resulting deformation gradient **F** in equation (60) and the momentum balance in equation (64). In order to accomplish this, a constitutive model is required which relates **F** to **P**. This relationship is provided through a Neo-Hookean energy function of the following form:

$$\Psi(\mathbf{F}) = \frac{\mu}{2} \left(\mathbf{F} : \mathbf{F}^T - 2 \right) - \mu \ln(J) + \frac{\lambda}{2} (\ln(J))^2$$
(65)

The definition of \mathbf{P} is

$$\mathbf{P} = \frac{d\Psi}{d\mathbf{F}} = \lambda \ln(J)\mathbf{F}^{-T} + \mu(\mathbf{F} - \mathbf{F}^{-T})$$
(66)

where the following result has been used:

$$\frac{dJ}{d\mathbf{F}} = J\mathbf{F}^{-T} \tag{67}$$

Equations (60), (63) and (66) are combined to obtain an expression for **P**. The result is

$$\mathbf{P} = \mu \mathbf{Q} \cdot \mathbf{q} \cdot \mathbf{a} \cdot \mathbf{q}^T \tag{68}$$

where

$$\mathbf{a} = (\mathbf{f} - \mathbf{f}^{-T}) = Rg \frac{dh}{dR} (\mathbf{E}_2 \otimes \mathbf{E}_1 + \mathbf{E}_1 \otimes \mathbf{E}_2)$$
(69)

The divergence of **P** is computed as follows:

$$\nabla_0 \cdot \mathbf{P} = \frac{\partial \mathbf{P}}{\partial R} \cdot \mathbf{E}_R + \frac{1}{R} \frac{\partial \mathbf{P}}{\partial \Theta} \cdot \mathbf{E}_{\Theta}$$
 (70)

The partial derivative in the first term of (70) is obtained using equation (68). The result is

$$\frac{\partial \mathbf{P}}{\partial R} = \mu \left(\frac{\partial \mathbf{Q}}{\partial R} \cdot \mathbf{q} \cdot \mathbf{a} \cdot \mathbf{q}^T + \mathbf{Q} \cdot \frac{\partial \mathbf{q}}{\partial R} \cdot \mathbf{a} \cdot \mathbf{q}^T + \mathbf{Q} \cdot \mathbf{q} \cdot \frac{\partial \mathbf{a}}{\partial R} \cdot \mathbf{q}^T + \mathbf{Q} \cdot \mathbf{q} \cdot \mathbf{a} \cdot \frac{\partial \mathbf{q}^T}{\partial R} \right)$$
(71)

Since $\partial \mathbf{q}/\partial R = \mathbf{0}$, equation (71) is reduced to the following:

$$\frac{\partial \mathbf{P}}{\partial R} = \mu \left(g \frac{dh}{dR} \mathbf{A} \cdot \mathbf{Q} \cdot \mathbf{q} \cdot \mathbf{a} \cdot \mathbf{q}^T + g \left(\frac{dh}{dR} + R \frac{d^2h}{dR^2} \right) \mathbf{Q} \cdot \mathbf{q} \cdot \left(\mathbf{E}_2 \otimes \mathbf{E}_1 + \mathbf{E}_1 \otimes \mathbf{E}_2 \right) \cdot \mathbf{q}^T \right)$$
(72)

The first term in equation (70) is computed using equation (72). The result is

$$\frac{\partial \mathbf{P}}{\partial R} \cdot \mathbf{E}_R = \mu \left(R \left(g \frac{dh}{dR} \right)^2 \mathbf{A} \cdot \mathbf{Q} \cdot \mathbf{q} \cdot \mathbf{E}_2 + g \left(\frac{dh}{dR} + R \frac{d^2h}{dR^2} \right) \mathbf{Q} \cdot \mathbf{q} \cdot \mathbf{E}_2 \right)$$
(73)

The partial derivative in the second term of equation (70) is obtained using equation (68). The result is

$$\frac{1}{R}\frac{\partial \mathbf{P}}{\partial \Theta} = \frac{\mu}{R}\left(\frac{\partial \mathbf{Q}}{\partial \Theta} \cdot \mathbf{q} \cdot \mathbf{a} \cdot \mathbf{q}^T + \mathbf{Q} \cdot \frac{\partial \mathbf{q}}{\partial \Theta} \cdot \mathbf{a} \cdot \mathbf{q}^T + \mathbf{Q} \cdot \mathbf{q} \cdot \frac{\partial \mathbf{a}}{\partial \Theta} \cdot \mathbf{q}^T + \mathbf{Q} \cdot \mathbf{q} \cdot \mathbf{a} \cdot \frac{\partial \mathbf{q}^T}{\partial \Theta}\right)$$
(74)

Since $\partial \mathbf{Q}/\partial \Theta = \mathbf{0}$ and $\partial \mathbf{a}/\partial \Theta = \mathbf{0}$, equation (74) reduces to the following:

$$\frac{1}{R}\frac{\partial \mathbf{P}}{\partial \Theta} = \frac{\mu}{R} \left(\mathbf{Q} \cdot \mathbf{A} \cdot \mathbf{q} \cdot \mathbf{a} \cdot \mathbf{q}^T + \mathbf{Q} \cdot \mathbf{q} \cdot \mathbf{a} \cdot \mathbf{A}^T \cdot \mathbf{q}^T \right)$$
(75)

Equation (75) is combined with equation (69) along with the fact that $\mathbf{A}^T \cdot \mathbf{E}_2 = \mathbf{E}_1$ in order to provide the following expression for the second term in equation (70). The result is

$$\frac{1}{R}\frac{\partial \mathbf{P}}{\partial \mathbf{\Theta}} \cdot \mathbf{E}_{\mathbf{\Theta}} = \mu g \frac{dh}{dR} \left(\mathbf{Q} \cdot \mathbf{A} \cdot \mathbf{q} \cdot \mathbf{E}_1 + \mathbf{Q} \cdot \mathbf{q} \cdot \mathbf{E}_2 \right)$$
 (76)

The transformation tensor to the deformed coordinates is

$$\mathbf{r} = \mathbf{Q} \cdot \mathbf{q} = \begin{pmatrix} \cos(\theta) & -\sin(\theta) & 0\\ \sin(\theta) & \cos(\theta) & 0\\ 0 & 0 & 1 \end{pmatrix}$$
(77)

where

$$\theta = \Theta + \alpha(R, t) \tag{78}$$

Equation (77) is substituted into equations (73) and (76) to produce the following results:

$$\frac{\partial \mathbf{P}}{\partial R} \cdot \mathbf{E}_{R} = \mu \left(R \left(g \frac{dh}{dR} \right)^{2} \mathbf{A} \cdot \mathbf{r} \cdot \mathbf{E}_{2} + g \left(\frac{dh}{dR} + R \frac{d^{2}h}{dR^{2}} \right) \mathbf{r} \cdot \mathbf{E}_{2} \right)$$
(79)

$$\frac{1}{R}\frac{\partial \mathbf{P}}{\partial \Theta} \cdot \mathbf{E}_{\Theta} = \mu g \frac{dh}{dR} (\mathbf{A} \cdot \mathbf{r} \cdot \mathbf{E}_1 + \mathbf{r} \cdot \mathbf{E}_2)$$
(80)

The relationships, $\mathbf{A} \cdot \mathbf{r} = \mathbf{r} \cdot \mathbf{A}$, $\mathbf{A} \cdot \mathbf{E}_2 = -\mathbf{E}_1$ and $\mathbf{A} \cdot \mathbf{E}_1 = \mathbf{E}_2$ are combined with equations (79), (80) and (70). The result is

$$\nabla_0 \cdot \mathbf{P} = \mu g \left(3 \frac{dh}{dR} + R \frac{d^2 h}{dR^2} \right) \mathbf{r} \cdot \mathbf{E}_2 - \mu R \left(g \frac{dh}{dR} \right)^2 \mathbf{r} \cdot \mathbf{E}_1$$
 (81)

which reduces to the following:

$$\nabla_0 \cdot \mathbf{P} = -\mu R \left(g \frac{dh}{dR} \right)^2 \mathbf{E}_r + \mu g \left(3 \frac{dh}{dR} + R \frac{d^2h}{dR^2} \right) \mathbf{E}_{\theta}$$
 (82)

The velocity \mathbf{v} is obtained using equations (51), (54) and the chain rule. The result is

$$\mathbf{v} = \dot{\mathbf{x}} = Rh \frac{dg}{dt} \mathbf{Q} \cdot \mathbf{E}_{\Theta} \tag{83}$$

The following expression for the acceleration is obtained from equation (83).

$$\mathbf{a} = \dot{\mathbf{v}} = -R \left(h \frac{dg}{dt} \right)^2 \mathbf{Q} \cdot \mathbf{E}_R + Rh \frac{d^2g}{dt^2} \mathbf{Q} \cdot \mathbf{E}_{\Theta}$$
 (84)

Use of the relationships $\mathbf{E}_R = \mathbf{q} \cdot \mathbf{E}_1$ and $\mathbf{E}_{\Theta} = \mathbf{q} \cdot \mathbf{E}_2$ reduce equation (84) to the following:

$$\mathbf{a} = -R\left(h\frac{dg}{dt}\right)^2 \mathbf{E}_r + Rh\frac{d^2g}{dt^2} \mathbf{E}_{\theta} \tag{85}$$

Equations (64), (82) and (85) are combined to solve for $\mathbf{b}(R, \Theta, t)$. The result is

$$\mathbf{b} = \left(-R\left(h\frac{dg}{dt}\right)^2 + \frac{\mu}{\rho_0}R\left(g\frac{dh}{dR}\right)^2\right)\mathbf{E}_r + \left(Rh\frac{d^2g}{dt^2} - \frac{\mu}{\rho_0}g\left(3\frac{dh}{dR} + R\frac{d^2h}{dR^2}\right)\right)\mathbf{E}_\theta \tag{86}$$

The specific form of h(R) is selected based on the selected annulus geometry of $R_a = 3/4$ and $R_b = 5/4$. The expression for h(R) is

$$h(R) = (16(R-1)^2 - 1)^2 (87)$$

It is easily verified that the form in equation (87) satisfies h(3/4) = h(5/4) = 0 and dh/dR(3/4) = dh/dR(5/4) = 0. The specific form of g(t) is

$$g(t) = \frac{1}{2}(1 - \cos(2\pi t)) \tag{88}$$

which satisfies g(0) = 0 and dg/dt(0) = 0. The function forms of h(R) and g(t) in equations (87) and (88) lead to analytical expressions for $\mathbf{P} = \mathbf{P}(R, \Theta, t)$ and $\mathbf{v} = \mathbf{v}(R, \Theta, t)$ that result in the following convenient initial and boundary conditions for the problem:

$$\mathbf{v}(1/4, \mathbf{\Theta}, t) = \mathbf{v}(5/4, \mathbf{\Theta}, t) = \mathbf{0}$$
(89)

$$\mathbf{P}(1/4, \mathbf{\Theta}, t) = \mathbf{P}(5/4, \mathbf{\Theta}, t) = \mathbf{0} \tag{90}$$

$$\mathbf{v}(R,\Theta,0) = \mathbf{0} \tag{91}$$

Finally, equations (87) and (88) are substituted into equation (86) to obtain the analytical form of the components of $\mathbf{b} = b_r \mathbf{E}_r + b_\theta \mathbf{E}_\theta$. The result is

$$b_{r} = -\pi^{2} \sin^{2}(2\pi t) R \left(16(R-1)^{2} - 1\right)^{4} + \frac{\mu}{4\rho_{0}} \left(1 - \cos(2\pi t)\right)^{2} R \left(1024(R-1)^{3} - 64(R-1)\right)^{2}$$

$$b_{\theta} = 2\pi^{2} \cos(2\pi t) R \left(16(R-1)^{2} - 1\right)^{2} - \frac{\mu}{2\rho_{0}} \left(1 - \cos(2\pi t)\right) 64 \left(96R^{3} - 240R^{2} + 188R - 45\right)$$
(93)

References

- [1] Bishop, J.E., and Strack, O.E. A statistical method for verifying mesh convergence in Monte Carlo simulations with application to fragmentation. *International Journal for Numerical Methods in Engineering* 2011; **88**: 279-306.
- [2] Strack, O.E., Leavy, R.B. and Brannon, R.M. Aleatory uncertainty and scale effects in computational damage models for failure and fargmentation. *International Journal for Numerical Methods in Engineering* (2014). Published online. DOI: 10.1002/nme.4699
- [3] McGlaun, J.M., Thompson, S.L. and Elrick, M.G. CTH: A three-dimensional shock wave physics code. In: Proceedings of 1989 hypervelocity impact symposium
- [4] Benson, D.J. Computational methods in Lagrangian and Eulerian hydrocodes. *Computer Methods in Applied Mechanics and Engineering* 1992; **99**: 235-394.
- [5] Peery, J.S. and Carroll, D.E. Multi-Material ALE methods in unstructured grids. *Computer Methods in Applied Mechanics and Engineering* 2000; **187**: 591-619.
- [6] Sulsky, D., Zhou, .S-J and Schreyer, H.L. A particle method for history-dependent materials. *Computer Methods in Applied Mechanics and Engineering* 2000; **118**: 179-196.
- [7] van Leer, B. Towards the ultimate conservative difference scheme. IV. A new approach to numerical convection. *Journal of Computational Physics* 1977; **23**: 276-299.
- [8] Dukowicz, J.K. and Baumgardner, J.R. Incremental remapping as a transport/advection algorithm. *Journal of Computational Physics* 2000; **160**: 318-335.
- [9] Hill, R.N. and Szmelter, J. A multidimensional positive definite remapping algorithm for arbitrary Lagrangian-Eulerian methods. *International Journal for Numerical Methods in Fluids* 2011; **65**: 1338-1350.
- [10] Margolin, L.G. and Shashkov, M. Second-order sign-preserving conservative interpolation (remapping) on general grids. *Journal of Computational Physics* 2003; **1843**: 266-298.
- [11] Colella, P. The piecewise parabolic method (PPM) for gas-dynamical simulations. *Journal of Computational Physics* 1984; **54**: 174-201.
- [12] Dolbow, J., Mosso, S., Robbins, J. and Voth, T. Coupling volume-of-fluid based interface reconstructions with the extended finite element method. *Computer Methods in Applied Mechanics and Engineering* 2008; **197**: 439-477.
- [13] Mosso, S., Garasi, C. and Drake, R. A smoothed two-and three-dimensional interface reconstruction method. *Computing and Visualization in Science* 2009; **12**: 365-381.
- [14] Robinson, A.C. et al. ALEGRA: An arbitrary Lagrangian-Eulerian multimaterial, multiphysics code. Reno, Nevada, January 2008. Proceedings of the 46th AIAA Aerospace Sciences Meeting. AIAA-2008-1235.

- [15] Robinson, A.C., et. al.: ALEGRA User Manual. Technical Report SAND2014-1236, Sandia National Laboratories, Albuquerque, NM, February 2014
- [16] Vitali, E. and Benson, D.J. Modeling localized failure with arbitrary Lagrangian Eulerian methods. *Computational Mechanics* 2012; **49**: 197-121.
- [17] Sadeghirad, A., Brannon, R. and Burghardt, J. A convected particle domain interpolation technique to extend applicability of the material point method for problems involving massive deformation. *International Journal for Numerical Methods in Engineering*, 2011; **86**: 1435-1456.
- [18] Love, E., Rider, W.J. and Scovazzi, G. Stability analysis of a predictor/multi-corrector method for staggered-grid lagrangian shock hydrodynamics. *Journal of Computational Physics* 2009; **228**: 7543-7564.
- [19] Love, E. and Wong, M.K.: Lagrangian Continuum Dynamics in ALEGRA. Technical Report SAND2007-8104, Sandia National Laboratories, Albuquerque, NM, 87185
- [20] Rider, W.J., Love, E., Wong, M.K., Strack, O.E, Petney, S.V. and Labreche, D.A. Adaptive methods for multi-material ALE hydrodynamics. *International Journal for Numerical Methods in Engineering* 2011; **65**: 1325-1337.
- [21] Strang, G. On the construction and comparison of difference schemes. *SIAM Journal on Numerical Analysis* 1968; **5**: 506-517.
- [22] Robinson, A.C., Ketcheson, D.I., Ames, T.I. and Farnsworth, G.V.: A comparison of Lagrangian/Eulerian approaches for tracking the kinematics of high deformation solid motion. Technical Report SAND2009-5154, Sandia National Laboratories, Albuquerque, NM, September 2009
- [23] Johnson, G., and Cook, W. Fracture characteristics of three metals subjected to various strains, strain rates, temperatures, and pressures. *Engineering Fracture Mechanics*, 1985; **21**: 31-48.
- [24] Knupp, P. and Salari, K.: Verification of Computer Codes in Computational Science and Engineering Chapmann and Hall CRC, London (2003)
- [25] Kamojjala, K., Brannon, R., Sadeghirad, A. and Guilkey, J. Verification tests in solid mechanics. *Engineering with Computers*, published online 24 November 2013, DOI 10.1007/s00366-013-0342
- [26] Grady, D., and Benson, D. Fragmentation of metal rings by electromagnetic loading. *Experimental Mechanics* 1983; **23**: 393-400.
- [27] Strack, O.E., Leavy, R.B. and Brannon, R.M. Aleatory uncertainty and scale effects in computational damage models for failure and fragmentation. *International Journal for Numerical Methods in Engineering* 2015; **102**: 468-495.

[28] Johnson, G., and Cook, W. A constitutive model and data for metals subjected to large strains, high strain rates, and high temperatures. *The Seventh International Symposium of Ballistics*, The Hague, The Netherlands, 1983.

DISTRIBUTION:

1 R.L. Doney
 U.S. Army Research Laboratory
 ATTN: RDRL-WMP-D
 Aberdeen Proving Ground, MD, 21005
 (electronic copy)

J.R. Houskamp
 U.S. Army Research Laboratory
 ATTN: RDRL-WMP-D
 Aberdeen Proving Ground, MD, 21005
 (electronic copy)

1 R.B. Leavy U.S. Army Research Laboratory ATTN: RDRL-WMP-C

Aberdeen Proving Ground, MD, 21005 (electronic copy)

1	MS 1318	Erik Strack (electronic copy), 01426
1	MS 1323	Glen Hansen (electronic copy), 01443
1	MS 1323	Chris Luchini (electronic copy), 01443
1	MS 1323	John Niederhaus (electronic copy), 01446
1	MS 1323	Sharon Petney (electronic copy), 01443
1	MS 1323	Allen Robinson (electronic copy), 01443
1	MS 1323	Jason Sanchez (electronic copy), 01443
1	MS 0840	Steve Attaway (electronic copy), 01555
1	MS 0840	Kevin Ruggirello (electronic copy), 01555
1	MS 0899	Technical Library (electronic copy), 9536

